1   **Revision 3**

2   **Phase relations in the system FeCO$_3$-CaCO$_3$ at 6 GPa and 900-**

3   **1700 °C and its relation to the system CaCO$_3$-FeCO$_3$-MgCO$_3$**

4

5   Anton Shatskiy[1,2*], Yuri M. Borzdov[1], Konstantin D. Litasov[1,2], Igor N. Kupriyanov[1],

6   Eiji Ohtani[3], Yuri N. Palyanov[1,2]

7   [1]V.S. Sobolev Institute of Geology and Mineralogy, Russian Academy of Science,

8   Siberian Branch, Koptyuga pr. 3, Novosibirsk 630090, Russia

9   [2]Novosibirsk State University, Novosibirsk 630090, Russia

10   [3]Department of Earth and Planetary Material Science, Tohoku University, Sendai

11   980-8578, Japan

12

13   **Abstract**

14   The subsolidus and melting phase relations in the CaCO$_3$-siderite system have

15   been studied in multianvil experiments using graphite capsules at pressure of 6 GPa

16   and temperatures of 900-1700 °C. At low temperatures, the presence of ankerite splits

17   the system into two partial binaries: siderite + ankerite at 900 °C and ankerite +

18   aragonite up to 1000 °C. Extrapolated solvus curves intersect near 50 mol% just

19   below 900 °C. At 1100 and 1200 °C, the components appear to form single-phase

20   solid solutions with space group symmetry $R\bar{3}c$, while CaCO$_3$ maintains aragonite

21   structure up to 1600 °C and 6 GPa. The FeCO$_3$ solubility in aragonite does not exceed

22   1.0 and 3.5 mol% at 900-1000 and 1600 °C, respectively. An increase of FeCO$_3$

23   content above the solubility limit at $T > 1000$ °C, leads to composition-induced phase

24   transition in CaCO$_3$ from aragonite, $Pmcn$, to calcite, $R\bar{3}c$, structure. I.e., the presence

25   of FeCO$_3$ widens the calcite stability field down to the PT-conditions of sub-cratonic

1

26   mantle. The siderite-$CaCO_3$ diagram resembles a minimum type of solid solutions.

27   The melting loop for the $FeCO_3$-$CaCO_3$ join extends from 1580 ºC ($FeCO_3$) to

28   1670 °C ($CaCO_3$) through a liquidus minimum near 1280 ± 20 °C and 56 ± 3 mol%

29    $CaCO_3$. At X(Ca) = 0-30 mol%, 6 GPa and 1500-1700 ºC, siderite melts and dissolves

30   incongruently according to the reaction: siderite = liquid + fluid. The apparent

31   temperature and X(Ca) range of siderite incongruent dissolution would be determined

32   by the solubility of molecular CO_2 in $(Fe,Ca)CO_3$ melt.

33   The compositions of carbonate crystals and melts from the experiments in the

34   low-alkali carbonated eclogite (Hammouda 2003; Yaxley and Brey 2004) and

35   peridotite (Dasgupta and Hirschmann 2007; Brey et al. 2008) systems are broadly

36   consistent with the topology of the melting loop in the $CaCO_3$-$MgCO_3$-$FeCO_3$ system

37   at 6 GPa pressure: a Ca-rich dolomite-ankerite melt coexists with Mg-Fe-calcite in

38   eclogites at CaO/MgO > 1 and Mg-dolomite melt coexists with magnesite in

39   peridotites at CaO/MgO < 1. However, in fact, the compositions of near solidus

40   peridotite-derived melts and carbonates are more magnesian than predicted from the

41    $(Ca,Mg,Fe)CO_3$ phase relations.

42

43   ***Key words***: siderite; $FeCO_3$; aragonite; ankerite; phase relations; Raman; high

44   pressure; Earth's mantle.

45   **Introduction**

46   Carbon is transported into the mantle through subduction mainly as carbonates

47   over hundreds of millions of years. Some of this carbon is released as CO_2 at shallow

48   depths via island arc volcanism (Sano and Williams 1996; Marty and Tolstikhin 1998).

49   Significantly more carbon, however, appears to be subducted into the deep mantle

50   (Hilton et al. 2002; Dasgupta and Hirschmann 2010). At mantle depths in the presence

2

51   of alkalis, carbonates could partially melt to form Na- and K-rich carbonatite melts

52   (Sweeney 1994; Yaxley and Brey 2004; Brey et al. 2011; Grassi and Schmidt 2011;

53   Kiseeva et al. 2012; Kiseeva et al. 2013; Litasov et al. 2013), similar to those found as

54   microinclusions in kimberlitic diamonds (Navon 1991; Schrauder and Navon 1994;

55   Kaminsky et al. 2009; Klein-BenDavid et al. 2009; Weiss et al. 2009; Zedgenizov et

56   al. 2009; Logvinova et al. 2011; Zedgenizov et al. 2011). At the same time, refractory

57   alkaline earth carbonates could remain in a solid state down to upper and even lower

58   mantle depths, as indicated by high-pressure experiments (Yaxley and Green 1994;

59   Hammouda 2003; Dasgupta et al. 2004; Litasov and Ohtani 2009; Litasov and Ohtani

60   2010) and findings of crystalline Ca-, Ca-Mg-, Mg- and Fe-carbonates within

61   kimberlitic diamonds (Meyer and McCallum 1986; Bulanova and Pavlova 1987;

62   Phillips and Harris 1995; Wang et al. 1996; Sobolev et al. 1997; Stachel et al. 2000).

63   Carbonate minerals may enter subduction zones incorporated in hydrothermally

64   altered basaltic crust, overlying marine sediments and underlying mantle lithosphere.

65   Neglecting the contribution of subducting mantle lithosphere, whose carbon content is

66   not well constrained, the dominant source of carbon entering the present-day trenches

67   is carbonate-bearing altered oceanic basalt (Dasgupta and Hirschmann 2010). Two-

68   thirds of the global CO_2 subduction is composed of low-temperature carbonate

69   precipitated as veins and present in vesicles in the upper volcanics of ocean-floor

70   basalt, and the remainder is in accreted sediments (Jarrard 2003). Nearly all of this

71   CO_2 occurs in the form of calcite (Alt and Teagle 1999; Jarrard 2003), while siderite

72   or ankerite are also found (Laverne 1993).

73   The evidence for the deep ($\geq$150 km depths) subduction of carbonates within the

74   ocean slabs comes from the findings of Ca-Mg carbonates associated with diamond in

75   CO_2-bearing inclusions in xenoliths from a forearc magmatic rock in southwest Japan

3

76   (Murakami et al. 2008). Another evidence originates from mineral inclusions in

77   Brazilian diamonds, which represent distinct CaO-TiO_2-SiO_2-rich carbonate-bearing

78   lithology (Joswig et al. 1999; Stachel et al. 2000; Kaminsky et al. 2001; Brenker et al.

79   2005; Hayman et al. 2005; Brenker et al. 2007; Zedgenizov et al. 2014). The inclusion

80   mineralogy requires exhumation of the rocks from the transition zone and lower

81   mantle (Stachel et al. 2000; Harte 2010). The carbon isotope signatures of the host

82   diamonds are consistent with surface derived carbon (Bulanova et al. 2010; Walter et

83   al. 2011; Zedgenizov et al. 2013), and link them to a subduction-related processes.

84   The major-element mineral chemistry and the elevated incompatible trace element

85   abundances are consistent with crystallization of the inclusions from Ca-rich

86   carbonatitic melts derived from subducted slab (Walter et al. 2008).

87   The deep subduction of carbonates is also evident from continental crust

88   exhumed from mantle depths. Coesite- and diamond-bearing ultrahigh-pressure

89   (UHP) metamorphic rocks (eclogites, gneisses, metapelites and marbles) contain

90   variable amounts of carbonates as rock-forming minerals and/or as inclusions in high-

91   pressure minerals (Sobolev and Shatsky 1990; Xu et al. 1992; Okay 1993;

92   Dobrzhinetskaya et al. 1995; Shatsky et al. 1995; Larsen et al. 1998; Dobrzhinetskaya

93   et al. 2006; Korsakov and Hermann 2006; Perraki et al. 2006). These rocks appear

94   along ancient plate boundaries and derived from carbonate-bearing rocks originally

95   formed close to the Earth's surface (Searle et al. 2001). Their mineral assemblages

96   and *PT* conditions require that they were subducted to the depths of 130-220 km (4-7

97   GPa) and then brought back to the surface (Searle et al. 2001; Dobretsov and Shatsky

98   2004; Yaxley and Brey 2004; Shatsky et al. 2006; Mikhno and Korsakov 2013).

99   Although Ca-Mg carbonates are the most important carbonate compounds

100 entering subduction zones, Fe-bearing carbonates (siderite [$FeCO_3$] and ankerite

4

101   [(Ca,Fe)CO$_3$]) are also important in basaltic compositions and various sediments e.g.

102   (Laverne 1993).

103   Since 1955, considerable attention has been directed toward study of the phase

104   diagrams of the carbonate systems. The ultimate goal of these studies is an

105   understanding of the phase relations in geologically important portions of the ternary

106   system CaCO$_3$-MgCO$_3$-FeCO$_3$, which include the compositions of most rock-forming

107   carbonates. Subsolidus experiments in the CaCO$_3$-MgCO$_3$ system at $P(CO_2) \leq 0.1$

108   GPa and 625-850 °C (Graf and Goldsmith 1955) and at $P(CO_2) = 0.1$-0.3 GPa and

109   500-900 °C (Harker and Tuttle 1955) in the CaCO$_3$-FeCO$_3$ system at $P(CO_2) = 0.2$-

110   0.4 GPa and 300-550 °C (Rosenberg 1963), and in the system CaCO$_3$-MgCO$_3$-FeCO$_3$

111   at $P(CO_2) = 0.2$-0.4 GPa and 350-550 °C (Rosenberg 1967) and at 1.5 GPa and 600-

112   800 ºC (Goldsmith et al. 1962) initiated this work. Later on experimental conditions

113   were extended to higher pressures and temperatures in order to study both the

114   subsolidus and melting phase relations in the CaCO$_3$-MgCO$_3$ system at 1 GPa and

115   900-1400 °C (Byrnes and Wyllie 1981) and at 3.0 GPa and 1100-1620 °C (Irving and

116   Wyllie 1975).

117   Since significant mantle processes involving carbonates, such as diamond-grade

118   UHP metamorphism, mantle metasomatism, kimberlite magma generation, and

119   diamond formation, occur at the base of lithospheric mantle (150-230 km depths), 6

120   GPa is relevant pressure for a further study of the CaCO$_3$-MgCO$_3$-FeCO$_3$ system.

121   While the binary systems CaCO$_3$-MgCO$_3$ and MgCO$_3$-FeCO$_3$ have been recently

122   studied at 6 GPa and 800-1600 °C (Buob et al. 2006) and at 6 GPa and 900-1700 °C

123   (Shatskiy et al. 2014b), respectively (Fig. 1), the system CaCO$_3$-FeCO$_3$ has not yet

124   been studied at the PT conditions exceeding 2-3.5 GPa and 800-1100 °C (Davidson et

125   al. 1994; Franzolin et al. 2011). We present here the subsolidus and melting

5

126   relationships in the siderite-$CaCO_3$ at 6 GPa and 900-1700 ºC as a contribution to the

127   phase relations in the petrologically important ternary system $CaCO_3$-$MgCO_3$-$FeCO_3$.

128

129   **Experimental methods**

130   High-temperature experiments (1400-1700 ºC) were performed using Kawai-

131   type presses at Tohoku University (Sendai, Japan) (Shatskiy et al. 2011). We

132   employed a ZrO_2 pressure medium (PM) with edge length of 20.5 mm and WC anvils

133   with truncation edge length of 12 mm. Sample heating was achieved using a graphite

134   heater, 4.5/4.0 mm in outer/inner diameter and 11 mm in length. Sample temperature

135   was controlled using WRe(3/25%) thermocouple inserted in the heater center via

136   walls and electrically insulated by Al_2O_3 tubes (see Fig. 1a in Shatskiy et al. (2013b).

137   Low-temperature experiments (900-1300 ºC) were carried out using a pressless

138   split-sphere apparatus (BARS) in IGM SB RAS (Novosibirsk, Russia) (Palyanov et al.

139   2010; Shatskiy et al. 2011). In these experiments, we employed ZrO_2-based ceramics

140   as a PM shaped into a tetragonal prism (20.4×20.4×25.2 mm). The PM was

141   compressed by two anvils with 16×16 mm square truncations and four anvils with

142   16×20 mm rectangular truncations. Sample heating was achieved using a tubular

143   graphite heater, 13.0/12.0 mm in outer/inner diameter and 19.0 mm in height. The

144   sample temperature was controlled using PtRh(6/30) thermocouple inserted along

145   the heater axis (see Fig. 2 in Shatskiy et al. (2014a).

146   Mixtures of synthetic $CaCO_3$ with natural siderite, $Fe_{0.87}Mn_{0.06}Mg_{0.07}CO_3$ were

147   ground in an agate mortar under acetone and loaded into graphite cassettes (i.e.,

148   multiple sample holders). The Kawai cell assembly contained 16 samples, 0.9 mm in

149   diameter (see Fig. 3 in Shatskiy et al. (2014a). The BARS cell assembly contained 42

150   samples, 1.0 mm in diameter (see Fig. 2 in Shatskiy et al. (2014a). For this study we

6

151   used 7-9 holes with different sample compositions shown in Table 1. The remaining

152   holes were employed to study alternative carbonate systems. The loaded cassettes

153   were placed in a vacuum oven, heated to 240ºC for 1 hour then cooled to 130 °C and

154   stored for 8-12 hours prior to assembly preparation. Prepared assemblies were stored

155   at 130ºC in a vacuum oven for 1-2 hours prior to compression. During opening the

156   vacuum oven was filled with dry air rather than ambient air.

157   All experiments were performed as follows. The assemblies were compressed at

158   room temperature to pressure of 6 GPa, then the samples were heated to temperatures

159   ranging from 900 to 1700 °C. The temperature was maintained within 0.5 °C of the

160   desired value. The maximum temperature difference between samples did not exceed

161   20 °C (see Fig. 2 and 3 in Shatskiy et al. (2014a) and Fig. 3 in Shatskiy et al. (2013b).

162   Experiments were terminated by shutting off the electrical power of the heater,

163   followed by slow decompression.

164   Recovered samples were mounted into an epoxy resin and polished using 400-,

165   1000- and 1500-mesh sandpapers and 3-µm diamond past. We used low-viscosity

166   grade of epoxy, which can be drawn into pores and cracks by vacuum impregnation.

167   Samples were studied using a Tescan MYRA 3 LMU scanning electron microscope

168   coupled with an INCA Energy dispersive X-ray microanalysis system 450 equipped

169   with the liquid nitrogen-free Large area EDS X-Max-80 Silicon Drift Detector

170   (Oxford Instruments) at V.S. Sobolev IGM SB RAS (Novosibirsk, Russia). The EDS

171   spectra were collected by rastering the electron beam over a surface area available for

172   the analysis with linear dimensions from 10 to 300 µm at 20 kV accelerating voltage

173   and 1 nA beam current. Counting times for spectra and X-ray elemental map

174   collection were 20-30 seconds. No beam damage or change in measured composition

175   with time was observed when using the current setting. We also confirmed that the

7

176 size of the analyzed region has no measurable effect on the resulting data, as long as

177 the area is significantly larger than the grain size. The EDS spectra were optimized for

178 the quantification using standard XPP procedure included in the INCA Energy 450

179 software.

180 Raman measurements were performed using a Horiba J.Y. LabRAM HR800

181 Raman spectrometer equipped with an Olympus BX41 confocal microscope at the

182 V.S. Sobolev IGM SB RAS (Novosibirsk, Russia). Spectra were recorded at room

183 temperature with the 514 nm line of a CVI Melles Griot Ar-ion laser (~1 mW at the

184 sample) and spectral resolution of approximately 2 cm^{-1}. An Olympus 100×0.9

185 objective (100× magnification and a NA of 0.9) was used to focus the laser beam onto

186 the sample and to collect the Raman signal.

187

188 **Experimental results**

189 Representative backscattered electron (BSE) images of the run products

190 quenched at 900-1300 ºC (Fig. 2) and 1300-1700 ºC (Fig. 3) were used to delineate

191 the phase fields. Positions of the phase boundaries were verified according to the

192 electron microprobe analyses listed in Table 1 and identification of crystal phases by

193 Raman spectroscopy (Fig. 4). At 900 °C, samples are represented by crystal

194 aggregates of siderite (Ca# = 2 mol%) + ankerite (Ca# = 42 mol%) at X(Ca) = 20-40

195 mol% (Fig. 2a), ankerite (Ca# = 50 mol%) at X(Ca) = 50 mol% (Fig. 2b), and ankerite

196 (Ca# = 53 mol%) + aragonite (Ca# = 99-100 mol%) at X(Ca) = 60-90 mol% (Fig. 2c),

197 where Ca# = Ca/(Ca+Fe+Mn+Mg) is $CaCO_3$ mole content in the phases and X(Ca) is

198 $CaCO_3$ mole content in the starting mixture. At 1000 °C, the run products were

199 represented by a single-phase aggregate of siderite-ankerite solid solution at X(Ca) =

200 10-70 mol% (Fig. 2d), while the ankerite (Ca# = 79 mol%) + aragonite (Ca# = 95.5-

8

201   100 mol%) assemblage was established at X(Ca) = 80 and 90 mol% (Fig. 2e,f). At

202   1100 and 1200 °C, a single-phase aggregate of siderite-calcite solid solution appears

203   in whole compositional range, X(Ca) = 0-90 mol%. First melting was established at

204   1300 °C and X(Ca) = 30-70 mol%. The quenched liquid formed dendritic aggregate of

205   carbonate crystals at the high-temperature (HT) side of the capsules (Fig. 2j-i). On the

206   Fe-rich side of the system, the liquid has Ca# = 54 mol% and coexists with siderite-

207   ankerite solid solution with Ca# = 25 mol% (Fig. 2g,h). On the Ca-rich side, the liquid

208   has Ca# = 58 mol% and coexists with the ankerite-calcite solid solution with Ca# = 78

209   mol% (Fig. 2i). Liquid volume fraction increases successively, when X(Ca) changes

210   from 30 to 50 and from 70 to 60 mol% (Fig. 2g,h). At 1500 ºC and X(Ca) = 40-60

211   mol%, samples were completely melted (Table 1). At X(Ca) = 10-30 mol%, the liquid

212   (Ca# = 31 mol%) coexists with siderite (Ca# = 7 mol%) (Fig. 3a,c), whereas at X(Ca)

213   = 90 mol%, the liquid (Ca# = 82 mol%) coexists with calcite (Ca# = 94 mol%) (Fig.

214   3d, 4). At 1600 and 1620 ºC, complete melting was established at X(Ca) = 30-90 and

215   20-90 mol%, respectively. At the Fe-rich side, siderite (Ca# = 4 mol%) coexists with

216   liquid with Ca# = 22 and 18 mol% at 1600 and 1620 ºC, respectively. At the Ca-rich

217   side, aragonite (Ca# = 96.5 mol%) coexists with liquid with Ca# = 89 mol% (Fig. 3e,

218   4). While $CaCO_3$ was found to be solid at 1600 ºC (Fig. 3f), natural siderite

219    $Fe_{0.87}Mn_{0.06}Mg_{0.07}CO_3$, which we used as a starting material, melts partially to form

220    $Fe_{0.90}Mn_{0.06}Mg_{0.04}CO_3$ liquid and $Fe_{0.86}Mn_{0.06}Mg_{0.08}CO_3$ siderite (Fig. 3g). At 1700 ºC,

221   all studied compositions, X(Ca) = 0-90 mol%, melted completely (Fig. 3h,i). At 1500-

222   1700 ºC and X(Ca) ≤ 30 mol%, the quenched melt contains rounded voids, 50-100 μm

223   in diameter, and Fe oxide in form of tiny worms within the dendrite aggregate (Fig.

224   3a-b,h,i).

9

225   In the present study we used natural siderite containing 6 mol% $MnCO_3$ and 7

226   mol% $MgCO_3$. Although the obtained Fe-bearing carbonate phases exhibit uniform

227   Mn/(Fe+Mn+Mg) ratio, magnesium tends to disproportionate into the solid phase

228   (siderite) at melting, which extends the siderite stability field to higher temperatures.

229    $Fe_{0.87}Mn_{0.06}Mg_{0.07}CO_3$ undergoes partial melting at 1600 ºC and melts completely at

230   1700 ºC, whereas melting point of Mg-free $Fe_{0.94}Mn_{0.06}CO_3$ siderite was estimated to

231   be 1580 ºC (Shatskiy et al. 2014b). We also observed systematic increase of the Ca-

232   number in liquid and its simultaneous decrease in coexisting siderite with increasing

233   XCa in the system at fixed temperature. This observation can be attributed to the

234   deviation of siderite end-member from the pure $FeCO_3$ composition. The maximum

235   deviation, by 6-7 mol%, occurs at 1300 ºC and it diminishes to 2-3 mol% at 1500-

236   1600 ºC.

237   The selected Raman spectra of obtained carbonates are presented in Figure 4. In

238   the $(Ca,Fe)CO_3$ solid solutions with Ca# varying from 0 to 94 mol%, the band

239   positions of all the Raman-active modes match the values of calcite group of minerals

240   (Table 2, Fig. 4a-c). In contrast, the band positions of carbonates with Ca# = 97 and

241   100 mol% synthesized at 1600 °C resemble the aragonite Raman spectrum (Frech et

242   al. 1980; Kontoyannis and Vagenas 2000; Edwards et al. 2005) (Fig. 4d,e). The

243   assignments of the Raman modes are based on following references (Rutt and Nicola

244   1974; White 1974; Scheetz and White 1977; Edwards et al. 2005).

245   The Raman spectra of the $(Ca,Fe)CO_3$ solid solutions display four fundamental

246   vibrational modes of CO_3^{2-} ions (internal modes), namely, the symmetric stretching

247   vibration (v_1) at 1085-1089 cm^{-1}, an out-of-plane band (v_2) at 867-875 cm^{-1},

248   asymmetric stretching mode (v_3) at 1428-1448 cm^{-1}, and in-plane bending mode (v_4)

249   at 715-738 cm^{-1}. Two lattice vibration peaks are observed at low frequency (external

10

250   modes): a transitional mode at 157-188 cm^{-1} (T) and a librational mode at 279-288

251   cm^{-1} (L). Additionally, a very broad low intensity peak was seen in the region 501-

252   571 cm^{-1} at Ca# = 0-70 %. This band is almost certainly due to electronic Raman

253   scattering from the Fe^{2+} ion (Rutt and Nicola 1974). A weak line ($2v_2$) observed at

254   1727-1750 cm^{-1} (Fig 4, Table 2) corresponds to the combination of v_1 and v_4

255   (Gunasekaran et al. 2006; Boulard et al. 2012). As Ca# increases, the Raman band

256   positions shift to higher wavenumbers in the case of $2v_2$ mode and to lower

257   wavenumbers in the case of v_4 and T modes.

258   The Raman spectra of aragonite show a line at 1086 cm^{-1} in the v_1 region, a very

259   small peak at 854 cm^{-1} in the v_2 region, two low intensity peaks at 1574 and 1463 cm^{-1}

260   in the v_3 region, three lines at 717, 707 and 703 cm^{-1} in the v_4 region and a number of

261   low wavenumber bands at 285, 273, 262, 250, 207, 192, 181, 154, 143 and 114 cm^{-1}

262   in the lattice mode region (Fig 4d,e).

263

264   **Discussion**

265   ***The FeCO$_3$-CaCO$_3$ system at 6 GPa.*** Phase relationships in the system siderite-

266   CaCO$_3$ at 6 GPa are illustrated in Figure 5. At low temperatures, the presence of

267   ankerite splits the system into two partial binaries: siderite + ankerite at 900 °C and

268   ankerite + aragonite up to 1000 °C. Extrapolated solvus curves intersect near 50 mol%

269   just below 900 °C. This is consistent with data of Morlidge et al. (2006) where the

270   breakdown reaction of ankerite → aragonite + siderite occurs at 880 ºC at 6 GPa. At

271   1100 and 1200 °C, the components (Ca# = 0-90 mol%) appear to form single-phase

272   solid solutions with space group symmetry $R\bar{3}c$. The siderite-CaCO$_3$ diagram

273   resembles a minimum type of solid solutions. The thermal minimum in the liquidus

274   and solidus curves is established near 1280 °C and 56 mol% CaCO$_3$.

11

275   ***CaCO₃ melting and calcite-aragonite transition.*** At 6 GPa, CaCO$_3$ melts

276   between 1600 and 1700 °C. This is consistent with the study of Suito et al. (2001)

277   where CaCO$_3$ melts between 1630 and 1730 °C at 6.2 GPa and with the studies on

278   diamond growth and dissolution, where CaCO$_3$ melt was established at 1700-1750 °C

279   and 7 GPa (Pal'yanov et al. 1998; Khokhryakov and Pal'yanov 2000).

280   A number of studies on the calcite-aragonite transition performed using different

281   techniques revealed conflicting results (Fig. 6, see also Fig. 1 in Mirwald (1976). The

282   vast majority of experimental data including the study by Irving and Wyllie (1975) are

283   in remarkable agreement with the calcite-aragonite equilibrium curve calculated by

284   Redfern et al. (1989) based on their calorimetric measurements (see Fig. 5 in their

285   study). An extrapolation of these data to higher *PT* conditions suggests that the

286   disordered calcite-aragonite-melt triple point is located at 5-5.5 GPa (Irving and

287   Wyllie 1973). However, these results are in poor agreement with the *in situ* energy

288   dispersive X-ray diffraction study by Suito et al. (2001), in which disordered calcite

289   was observed at 6.2 GPa and 1230 °C and remained stable until melting (Fig. 6). In

290   our study the Raman spectra of the CaCO$_3$ samples synthesized at 6 GPa and 900-

291   1600 °C closely resemble the aragonite spectra. This is consistent with the results of

292   Buob (2003), who also detected aragonite in the CaCO$_3$ samples synthesized at 6 GPa

293   and 1300-1500 °C (page 77, section 6.2.1, Buob (2003). Thus, our data are in good

294   agreement with the majority of previous data, e.g. (Irving and Wyllie 1975; Redfern et

295   al. 1989), but disagree with the results of Mirwald (1976) and Suito et al. (2001). The

296   discrepancy could be attributed to a reverse transition of disordered calcite to

297   aragonite during quenching. Yet, it was reported that quenched specimens of

298   disordered calcite mainly consists of calcite I ($R\bar{3}c$) rather than aragonite (Suito et al.

299   2001). Therefore, we suggest that aragonite observed in our experiments is the

12

300   thermodynamically stable phase rather than phase formed during quenching.

301   Consequently at 6 GPa, aragonite remains stable phase of pure $CaCO_3$ up to the

302   melting temperature (Fig. 6).

303   ***FeCO$_3$ solubility in aragonite.*** Our data show that solubility of $FeCO_3$ in

304   aragonite does not exceed 1.0 and 3.5 mol% at 900-1000 and 1600 °C, respectively

305   (Table 1, Fig. 5). An increase of the $FeCO_3$ content above the solubility limit at $T >$

306   1000 °C, leads to the chemically induced phase transition in $CaCO_3$ from aragonite,

307   *Pmcn*, to calcite, $R\bar{3}c$, structure. Note, that in contrast to dolomite, whose ordering at

308   low temperatures lowers the symmetry to $R\bar{3}$, ankerite is fully disordered even at

309   lower temperatures along the entire range of the ankerite = siderite + aragonite

310   reaction (Morlidge et al. 2006). The low solubility of $FeCO_3$ in aragonite implies that

311   presence of iron component may extend the calcite stability field down to 190 km

312   depth.

313   Since Fe-bearing $CaCO_3$ does not hold the $R\bar{3}c$ structure at the Ca-rich side in

314   the studied temperature range, a two-phase field with aragonite (*Pmcn*) and Fe-calcite

315   ($R\bar{3}c$) has to be stable up to incongruent melting point (*Tp*) of Fe-calcite. *Tp*

316   corresponds to temperature of peritectic reaction: Fe-calcite = aragonite + liquid.

317   Above *Tp*, aragonite coexists with liquid up to melting of pure $CaCO_3$ aragonite.

318   ***FeCO$_3$ melting and decomposition.*** In the present study we used natural siderite

319   containing 6 mol% $MnCO_3$ and 7 mol% $MgCO_3$. Although the obtained Fe-bearing

320   carbonate phases exhibit uniform Mn/(Fe+Mn+Mg) ratio, magnesium tends to

321   disproportionate into the solid phase (siderite) at melting, which extends siderite

322   stability field to higher temperatures. We found that $Fe_{0.87}Mn_{0.06}Mg_{0.07}CO_3$ undergoes

323   partial melting at 1600 ºC and melts completely at 1700 ºC, whereas melting point of

324   Mg-free siderite is about 1580 ºC (Shatskiy et al. 2014b) (Fig. 1a).

13

325   Development of minor Fe oxide and bubbles within siderite dendritic aggregate

326   (Fig. 3a,c,h,i) shows that either the reaction

327   siderite ($FeCO_3$) = liquid ($FeCO_3+Fe_3O_4$) + fluid (CO_2) + graphite or solute

328   carbon (C)   (1)

329   or

330   siderite ($FeCO_3$) = liquid ($FeCO_3+FeO$) + fluid (CO_2)   (2)

331   occur at $X(Ca)$ = 0-30 mol%, 6 GPa and 1500-1700 ºC. The apparent temperature and

332    $X(Ca)$ range of siderite incongruent dissolution would be determined by the solubility

333   of molecular CO_2 in $(Fe,Ca)CO_3$ melt. For example, the maximum CO_2 solubilities at

334   2.7 GPa in molten $CaCO_3$ and $MgCO_3$ achieve 23 and 12 mol%, respectively (Huang

335   and Wyllie 1976). The reactions (1) and (2) are described by the ternary Fe-C-O and

336   binary $FeO-CO_2$ systems, respectively. In both cases, the invariant point (Q) (where

337   incongruent melting begins) and singular point (S) (above which congruent melting

338   occurs) are located below and above 6 GPa and 1580 °C, respectively (Fig. 7a,d).

339   Note that established incongruent melting of $FeCO_3$ occurs at much higher pressures

340   than that of $CaCO_3$ and $MgCO_3$ (Wyllie and Tuttle 1960; Wyllie and Boettcher 1969;

341   Huang and Wyllie 1976). Irving and Wyllie (1975) suggested that calcite melts

342   incongruently below 0.1-0.7 GPa according to the reaction:

343   calcite ($CaCO_3$) = liquid ($CaCO_3+CaO$) + fluid (CO_2),   (3)

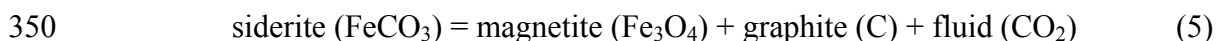344   whereas incongruent melting of magnesite occurs in the range of 2.3-2.7 GPa

345   according to the reaction:

346   magnesite ($MgCO_3$) = liquid ($MgCO_3+CO_2$) + periclase (MgO)   (4)

347   (Huang and Wyllie 1976). Previous phase equilibrium studies on siderite stability

348   were performed in the PT range of 0.05-1 GPa and 450-760 °C (Weidner 1972). At

349   these pressures, the invariant equilibrium:

14

350        $$\text{siderite (FeCO}_3) = \text{magnetite (Fe}_3\text{O}_4) + \text{graphite (C)} + \text{fluid (CO}_2) \qquad (5)$$

351   was established (Fig. 7a). The melting curve

352        $$\text{magnetite} + \text{graphite} = \text{liquid} + CO_2 \qquad (6)$$

353   was also determined in the range of 0.5-2 kbar and 880-950 °C (Weidner 1982)

354   (Fig. 7a). Assuming that Fe_3O_4 is stable at high temperatures, an extrapolation of

355   these data to higher pressures yields invariant melting point (Q) near 5 GPa and

356   1500 °C (Fig. 7a). Yet, we have no experimental proofs that Fe_3O_4 is stable near

357   melting temperature at pressures exceeding 3.5 GPa under redox conditions controlled

358   by the CCO buffer. The thermodynamic calculations reported by Sokol et al. (2010)

359   show that at 6.3 GPa the FeO-Fe_3O_4 buffer (WM) intersects the CCO buffer near

360   1300 °C. This temperature would be even lower (1100 °C) according to our recent

361   experimental data at 6 GPa (Shatskiy et al. 2014c). This implies that FeO rather than

362   Fe_3O_4 is stable above 1100-1300 °C at 6 GPa. The above ambiguity merits further

363   study of this system.

364   In the recent study by Tao et al. (2013) the experiments were performed in the

365   siderite system at 2.5-10 GPa using Pt capsules. Although their experiments were

366   conducted within the *PT* stability field of siderite (Fig. 7a), the run products contain

367   magnetite in addition to siderite (see Table 1 in Tao et al. (2013). As it was shown

368   previously, encapsulation of Fe-bearing samples in Pt ampoules accompanies by

369   absorption of iron by platinum (Merrill and Wyllie 1973; Ford 1978; Johannes and

370   Bode 1978) resulting in the sample oxidation (Gudmundsson and Holloway 1993;

371   Brey et al. 2008). Therefore in experiments reported by Tao et al. (2013) magnetite

372   appears owing to the ferrous iron disproportionation reaction:

373        $$4FeCO_3 \text{ (siderite)} = Fe^0 \text{ (Fe-Pt alloy)} + Fe_3O_4 \text{ (magnetite)} + 4CO_2 \text{ (fluid)}. \qquad (7)$$

15

374   Continuous increase of magnetite content in the run products with increasing run

375   duration, reported by Tao et al. (2013) (see Table 1 in their manuscript), is due to

376   continous increase of iron uptake by the Pt capsule with increasing temperature and

377   run duration (Johannes and Bode 1978). According to the experimental data of Tao et

378   al. (2013) at 6 GPa, siderite + magnetite assemblage does not melt up to 1400 ºC,

379   while magnetite coexisting with melt was established at 1450 ºC (Table 1 in (Tao et

380   al. 2013). Consequently, at 6 GPa, the $FeCO_3$-Fe_3O_4 eutectic (see Fig. 7d) is located

381   near 1425 ± 25 °C, which is about 150 °C lower than the siderite melting point

382   established at 6 GPa (Shatskiy et al. 2014b).

383   ***The $FeCO_3$-$CaCO_3$ system vs. pressure.*** Previous studies in the $FeCO_3$-$CaCO_3$

384   system have determined subsolidus phase relationships in the range of 0.2-3.5 GPa

385   and 350-1100 ºC (Goldsmith et al. 1962; Rosenberg 1963; Davidson et al. 1994;

386   Franzolin et al. 2011). These data do not exhibit any pressure effect on the phase

387   topology in the studied pressure range (Fig. 8). However, comparison of our results at

388   6 GPa (Fig. 5) with the previous lower pressure data (Fig. 8) indicates substantial

389   differences. Particularly, the broad solvus calcite-siderite, which closes at XCa = 30

390   mol% and 980 °C (Franzolin et al. 2011) does not appear at 6 GPa. Instead, two

391   partial binaries: siderite + ankerite at 900 °C and ankerite + aragonite up to 1000 °C

392   were established (Fig. 5). In their experiments at 3.5 GPa in double Pt-graphite

393   capsules, Franzolin et al. (2011) established complete solid solutions between $FeCO_3$

394   and $CaCO_3$ at 1000 ºC (Fig. 8), while at 6 GPa the single-phase solid solution area

395   shifts to 1100-1200 °C and its discontinuity brakes at the Ca-rich side due to

396   appearance of aragonite (Fig. 5). Franzolin et al. (2011) also found that at 1100 ºC at

397   the Fe-rich side, $Fe_{0.75}Ca_{0.25}CO_3$ is not stable anymore and breaks down according to

398   the reaction:

16

399          $2Fe_{0.75}Ca_{0.25}CO_3 = Fe_{0.5}Ca_{0.5}CO_3 + 1/3Fe_3O_4 + 1/6C + 5/6CO_2,$ (8)
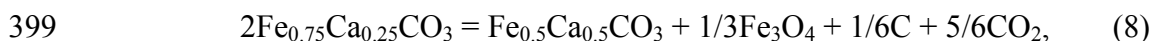
400   while complete miscibility between $Ca_{0.5}Fe_{0.5}CO_3$ and $CaCO_3$ still remains (Fig. 8). In

401   contrast at 6 GPa the incongruent reaction (8) involving magnetite is replaced by

402   incongruent dissolution of $FeCO_3$ in the $(Ca,Fe)CO_3$ melt according to the reaction (1)

403   or (2).

404   ***The CaCO₃-MgCO₃-FeCO₃ system at 6 GPa.*** The system $FeCO_3$-$MgCO_3$

405   shows continuous field of single phase solid solutions from 900 °C until melting (Fig.

406   1a). The extent of solid solutions is indicated by the trace of the solvus curves for the

407   systems $FeCO_3$-$CaCO_3$ (Fig. 5) and $MgCO_3$-$CaCO_3$ (Fig. 1b). In agreement with

408   theoretical predictions and lower pressure data (Fig. 3 in Rosenberg (1963), solid

409   solution increases when the radii of the cations are more similar. The topology of the

410   Fe-Ca and Mg-Ca diagrams are similar (Fig. 1b, 5). In both cases, the presence of

411   dolomite/ankerite splits the system into two partial binaries. The major difference in

412   the topology arises at the Ca-poor side. In the Mg-Ca system, the solidus intersects the

413   miscibility gap of disordered dolomite and magnesite, whereas in the Fe-Ca system,

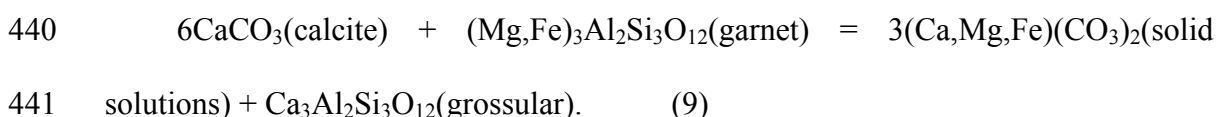414   the solvus ankerite-calcite closes below 1000 °C.

415   The subsolidus phase relations were also confirmed by the additional

416   experiments in the $FeCO_3$-$Ca_{0.5}Mg_{0.5}CO_3$ system. A single-phase solid solution field

417   is established in the range of 0-100 mol% $Ca_{0.5}Mg_{0.5}CO_3$ at 1100-1300 °C at 6 GPa,

418   while at 1000 °C the solid solution field is restricted by the range of 0-70 mol%

419    $Ca_{0.5}Mg_{0.5}CO_3$ (our unpublished data).

420   A possible topology of the ternary $FeCO_3$-$MgCO_3$-$CaCO_3$ system at 6 GPa is

421   shown in Figure 9. As can be seen, an addition of $FeCO_3$ to the $MgCO_3$-$CaCO_3$

422   system narrows the fields of two partial binaries and extends the single phase solid

423   solution field (Fig. 9c). At the same time, obtained data suggest a minor decrease in

17

424   the minimum melting temperature with adding geologically relevant amounts of

425   siderite or ankerite in the $MgCO_3$-$CaCO_3$ system, because the minimum melting

426   temperature of the $FeCO_3$-$CaCO_3$ system (~1280 ºC) is less than 100 °C lower than

427   that of $MgCO_3$-$CaCO_3$ (~1350 ºC) (Fig. 9b). Indeed, no melting occurs along the

428     $FeCO_3$-$Ca_{0.5}Mg_{0.5}CO_3$ join at 1300 °C and 6 GPa.

429   ***Implication for incipient melting in the upper mantle***
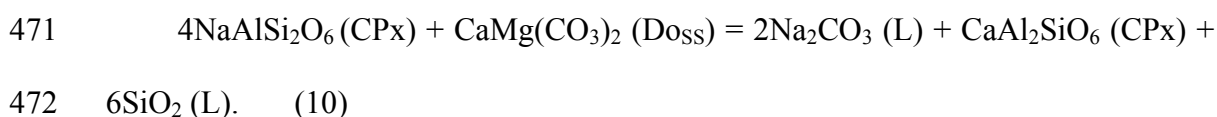
430   The solidus of anhydrous carbonated mantle is defined by the appearance of a

431   fusible carbonate. The carbonate composition is determined by the mantle lithology

432   (eclogite or peridotite) and by the PT conditions (Yaxley and Brey 2004; Brey et al.

433   2011; Grassi and Schmidt 2011; Litasov et al. 2013). Although CO_2 enters subduction

434   zones mainly in the form of calcite in hydrothermally altered basalts (Alt and Teagle

435   1999; Jarrard 2003), carbonates exhumed from the mantle depths are often dolomitic

436   in composition (Sobolev and Shatsky 1990; Murakami et al. 2008). This is because

437   calcite subjected to the PT conditions of eclogite facies as a part of basaltic oceanic

438   crust reacts with garnet to form $(Ca,Mg,Fe)CO_3$ solid solutions accordingly to the

439   reaction (Yaxley and Brey 2004):

440          $6CaCO_3$(calcite)   + $(Mg,Fe)_3Al_2Si_3O_{12}$(garnet)   = $3(Ca,Mg,Fe)(CO_3)_2$(solid

441   solutions) + $Ca_3Al_2Si_3O_{12}$(grossular).   (9)

442   The appearance of the $(Ca,Mg,Fe)CO_3$ solid solution (ss) in eclogite determines the

443   solidus temperatures and composition of incipient melting. Depending on the bulk

444   composition, particularly by the CaO/MgO molar ratio, either the Ca- or Mg-rich side

445   of the ternary $CaCO_3$-$FeCO_3$-$MgCO_3$ system determines the melting phase relations

446   (Table 3, Fig. 10). At CaO/MgO > 1, the calcite (Ct_{SS}) + garnet (Grt) + clinopyroxene

447   (CPx) + coesite (Co) assemblage coexists with the Ca-rich dolomite-ankerite melt,

448   (Hammouda 2003; Yaxley and Brey 2004), whereas at CaO/MgO < 1, the magnesite

18

449   (Mt_{SS}) + Grt + CPx assemblage coexists with the Ca-depleted dolomite-ankerite melt

450   (Dasgupta et al. 2004). Below the carbonated eclogite solidus at 6 GPa, the

451   crystallization sequence of carbonate minerals with increasing temperature is

452   aragonite + $(Ca,Mg,Fe)CO_3$ (ss) (900-950 °C) $\rightarrow$ $(Ca,Mg,Fe)CO_3$ (ss) (1000-1200 °C).

453   This is consistent with the $CaCO_3$-$FeCO_3$-$MgCO_3$ system topology (Fig. 9).

454   Extrapolation of the solidus of the YB04 carbonated eclogite (Table 3) (Yaxley

455   and Brey 2004) to 6 GPa suggests a solidus temperature of about 1340 °C, which

456   closely matches the minimum melting temperature of the $CaCO_3$-$MgCO_3$ binary

457   determined at 6 GPa (Buob et al. 2006). Yet, according to our results, the reported

458   Fe/(Mg+Fe) ratio of about 40-48 mol% in carbonates would lower melting

459   temperature to 1310 °C (Fig. 9). However, this small difference demonstrates rather

460   good convergence of the data than their discrepancy. On the other hand, the minimum

461   melting temperatures established for the $CaCO_3$-$MgCO_3$ (~1350 °C (Buob 2003)),

462    $Ca_{0.5}Mg_{0.5}CO_3$-$FeCO_3$ (>1300 °C) and $CaCO_3$-$FeCO_3$ (~1280 °C) systems are higher

463   than solidus temperatures of carbonated eclogite: H03 (~1225 °C at 6 GPa and 975 °C

464   at 6.5 GPa, (Hammouda 2003) and D04 (1080 °C at 6.1 GPa (Dasgupta et al. 2004).

465   Since Na_2O has a strong effect on partial melting in the carbonate systems (Shatskiy

466   et al. 2013a; Shatskiy et al. 2013c; Shatskiy et al. 2014c); this difference can be

467   attributed to the higher Na_2O content in the H03 and D04 compositions (see Table 3).

468   Although in the subsolidus runs Na is mostly hosted in jadeite in clinopyroxene,

469   across the solidus Na redistributes to the carbonatite melt according to the reaction

470   (Yaxley and Brey 2004):

471        $4NaAlSi_2O_6$ (CPx) + $CaMg(CO_3)_2$ (Do_{SS}) = $2Na_2CO_3$ (L) + $CaAl_2SiO_6$ (CPx) +

472    $6SiO_2$ (L).   (10)

19

473   In addition, the differences can be explained by the presence of H_2O in H03 (Table 3).

474   For example, insufficient sample drying can substantially (by 150-200 °C) lower the

475   eutectic temperatures of carbonate systems (Shatskiy et al. 2013c; Shatskiy et al.

476   2014a).

477   In contrast to eclogites that have Ca# = 30-50 mol%, peridotites are depleted

478   (Ca# ≈ 5 mol%) and their subsolidus assemblage includes olivine (Ol), orthopyroxene

479   (OPx), clinopyroxene (CPx), garnet (Grt), and magnesite (Mt_{SS}) (Dasgupta and

480   Hirschmann 2007; Brey et al. 2008). Although the Ca# in near solidus peridotite-

481   derived melt varies between 30-37 mol%, i.e. close to the minimum melt composition

482   in the $CaCO_3$-$MgCO_3$-$FeCO_3$ system; the Ca# in coexisting magnesite does not

483   exceed 2-4 mol% (Table 3, Fig. 10). In accordance with phase relations in the $CaCO_3$-

484    $MgCO_3$-$FeCO_3$ system, the solidus temperature of Mt_{SS} from the peridotite-CO_2

485   experiments exceeds 1500-1600 °C at 6 GPa (Fig. 9, 10), whereas the solidus of

486   carbonated peridotite is established between 1200-1300 °C at 6 GPa (Dasgupta and

487   Hirschmann 2006; Brey et al. 2008). Thus, the phase relations in carbonate portion of

488   the peridotite system cannot control the solidus of low-alkali natural carbonated

489   peridotite alone. Instead, following carbonate-silicate melting reaction has to be

490   involved to explain incipient melting of carbonated peridotite (Dasgupta and

491   Hirschmann 2007):

492        $CaMgSi_2O_6(CPx) + 2MgCO_3(Mt) = CaMg(CO_3)_2(L) + Mg_2Si_2O_6(OPx)$ (11)
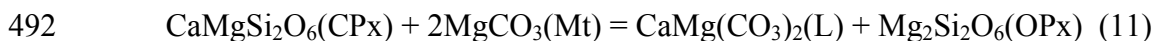
493   This reaction explains the extraction of the dolomitic carbonatite melt from

494   magnesite-bearing lherzolite. However, the solidus of carbonated peridotite is about

495   100 °C lower than the liquidus of the resulting melt if we consider the alkali-free

496    $CaCO_3$-$MgCO_3$-$FeCO_3$ system (Fig. 10). Since clinopyroxene is the major host for

497   Na_2O in the carbonated peridotite (Dasgupta and Hirschmann 2007), extraction of

20

498   sodium from clinopyroxene via reaction (10) produces Na_2CO_3, which has to lower

499   minimum melting of the $CaCO_3$-$MgCO_3$-$FeCO_3$ system (Shatskiy et al. 2013a;

500   Shatskiy et al. 2013c; Shatskiy et al. 2014c). Thus, the lower solidus temperature of

501   carbonated lherzolite in comparison to the $CaCO_3$-$MgCO_3$-$FeCO_3$ system can be

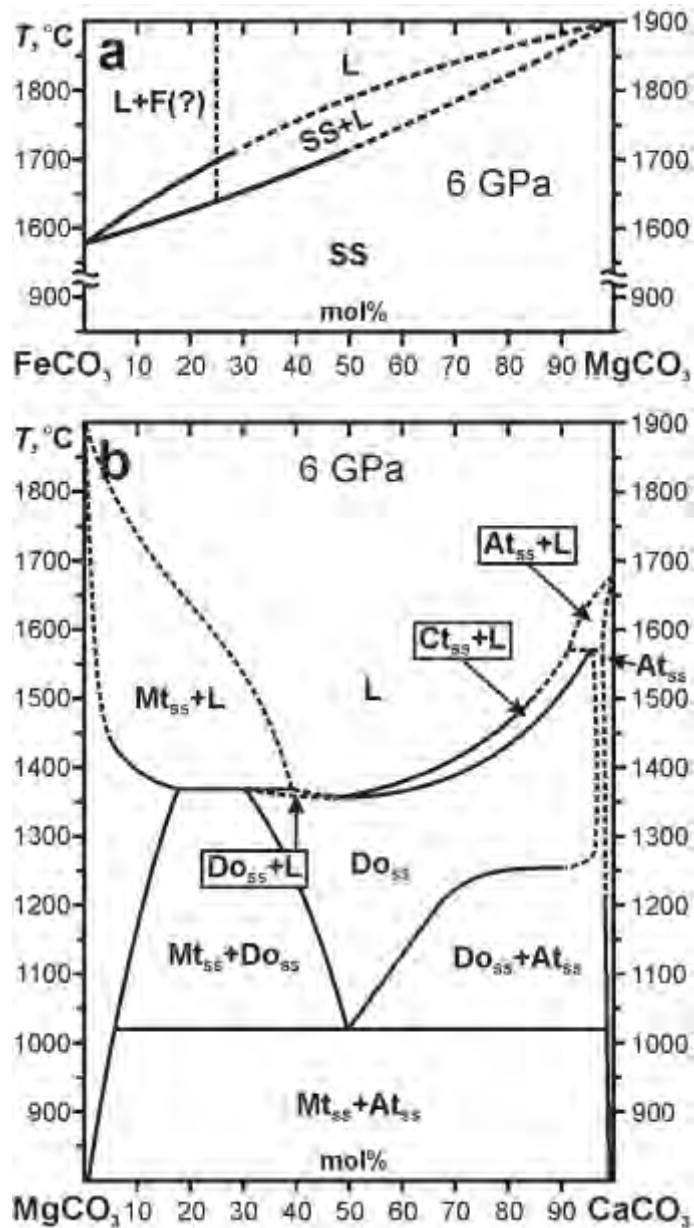502   explained by the fluxing effects of Na_2O (Na_2CO_3).

503

504   **Acknowledgements**

511

21

512

513   **Figure captions**

514

515   Fig. 1. Phase relations in the systems $FeCO_3$-$MgCO_3$ (a) and $MgCO_3$-$CaCO_3$ (b)

516   at 6 GPa. (a) and (b) modified after Shatskiy et al. (2014b) and Buob (2003),

517   respectively. The melting temperature of $CaCO_3$ is based on our and Suito et al.

518   (2001) experimental data. The melting point of $MgCO_3$ is obtained by extrapolation of

519   experimental data of Katsura and Ito (1990) who conducted $MgCO_3$ melting

520   experiments at 8 and 15 GPa. SS = $(Fe,Mg)CO_3$ solid solutions; Mt_{SS} = Ca-bearing

521   magnesite; Do_{SS} = $(Mg,Ca)CO_3$ solid solutions; Ct_{SS} = Mg-bearing calcite; At_{SS} =

522   Mg-bearing aragonite; L = liquid.

22

523
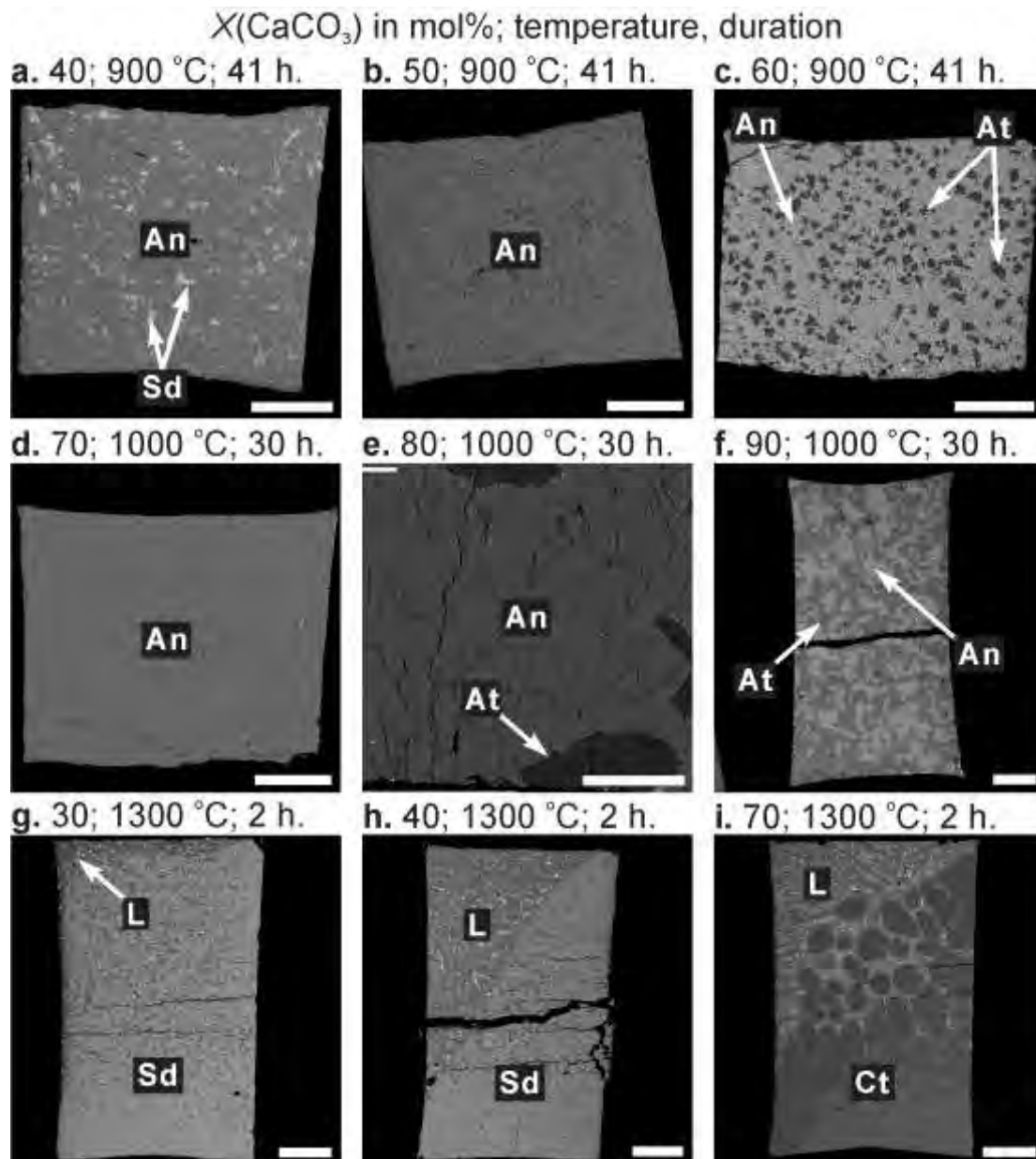
524

525   Fig. 2. Representative BSE images of sample cross-sections illustrating phase

526   relations in the system siderite-CaCO$_3$ at 6 GPa and 900-1300 °C. Sd = siderite; An =

527   ankerite; Ct = calcite; Ar = aragonite; L = liquid. Scale length is 200 μm.

23
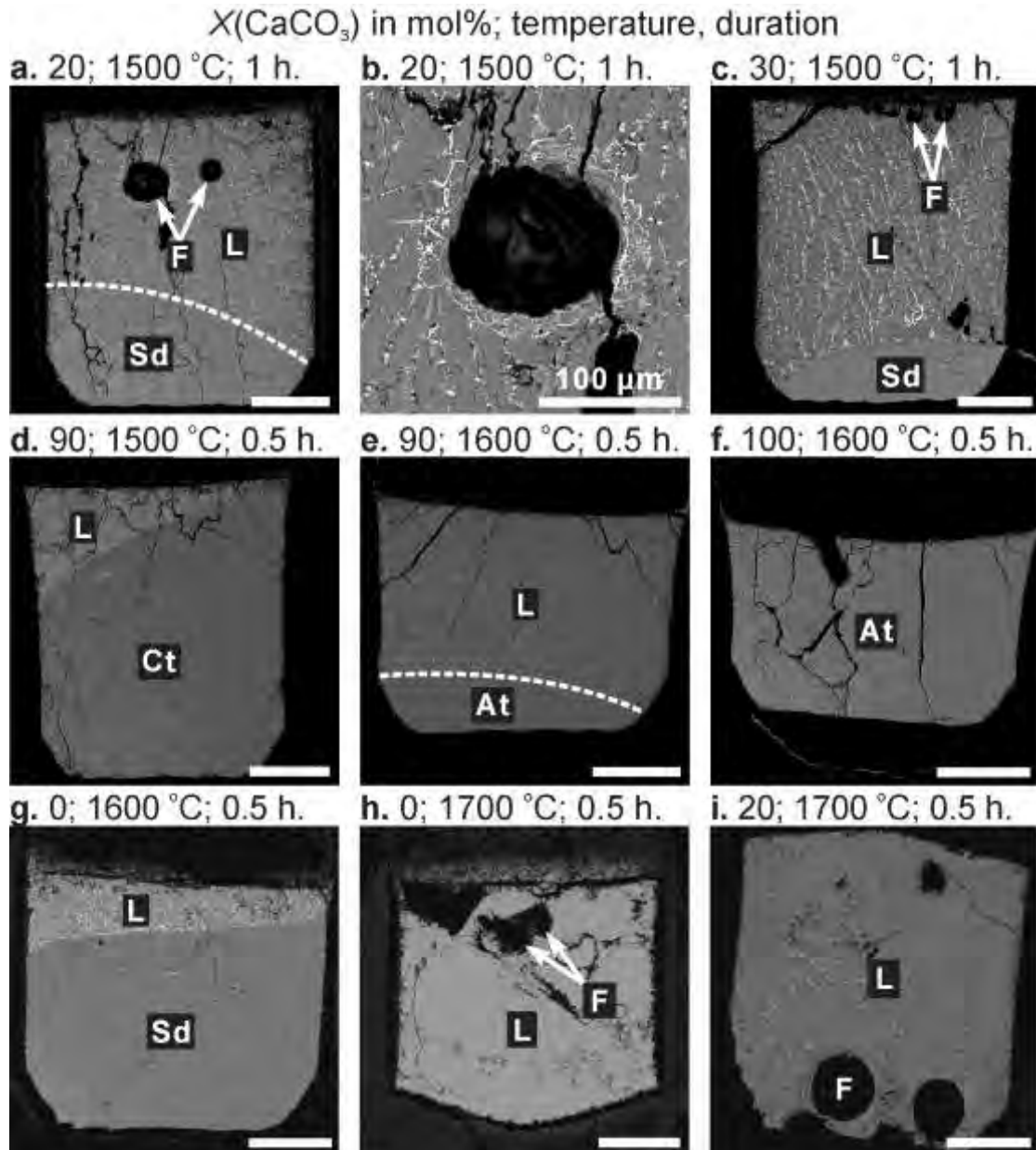
Fig. 3. Representative BSE images of sample cross-sections illustrating phase relations in the system siderite-$CaCO_3$ at 6 GPa and 1500-1700 °C. Sd = siderite; An = ankerite; Ct = calcite; Ar = aragonite; L = liquid; F = fluid. Scale length is 200 μm.

24

532
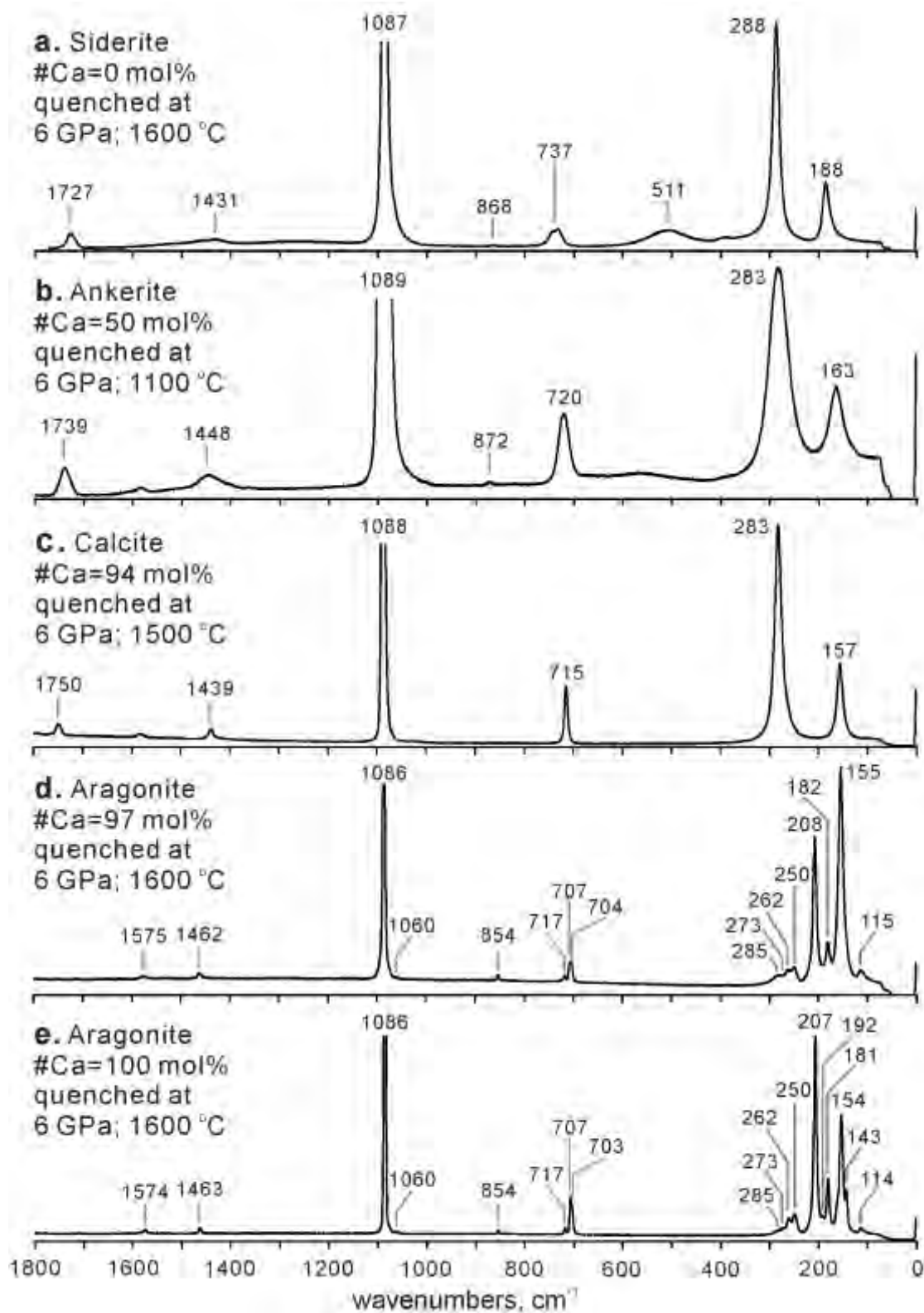
Fig. 4. Representative unpolarized Raman spectra of Ca-Mg carbonates
synthesized at 6 GPa in the system $Fe_{0.87}Mn_{0.06}Mg_{0.07}CO_3$-$CaCO_3$. The spectra were
collected at ambient conditions.

25

536

537
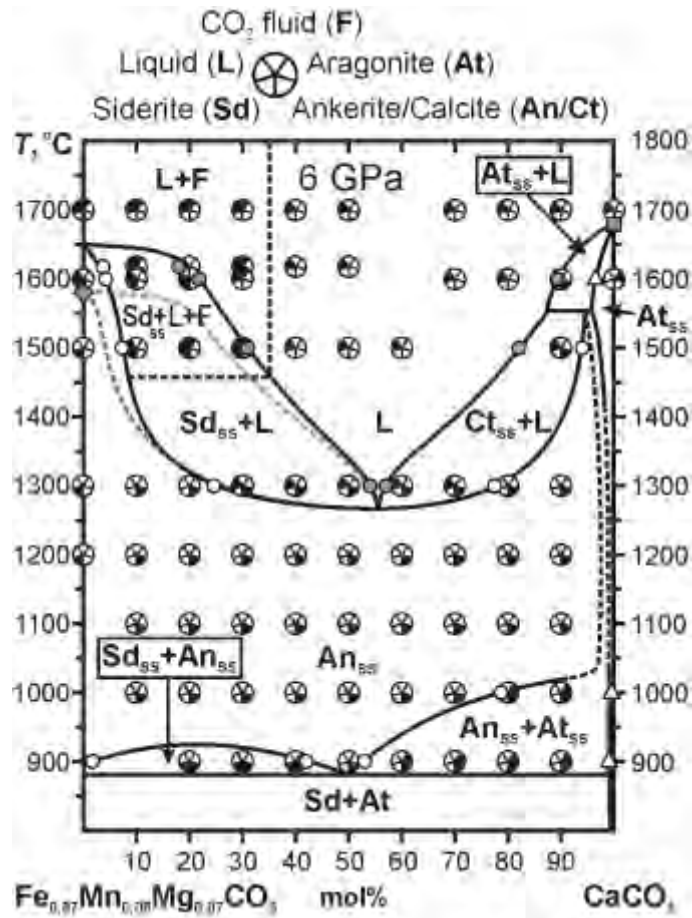
Fig. 5. Isobaric T-X diagram for the system siderite-$CaCO_3$ at 6 GPa. Grey and

opened circles mark melt and solid compositions measured by EDS. Grey rhomb

denotes $Fe_{0.96}Mn_{0.06}CO_3$ siderite melting point (Shatskiy et al. 2014b). Grey dashed

lines denote solidus and liquidus in the Mg-free system. Grey square denotes melting

point of $CaCO_3$ (Suito et al. 2001). Sd+At = An from (Morlidge et al. 2006). Sd =

siderite; Sd_{SS} = Ca-bearing siderite; An_{SS} = ankerite solid solution; Ct_{SS} = Fe-bearing

calcite; At = aragonite; At_{SS} = Fe-bearing aragonite.

545

26
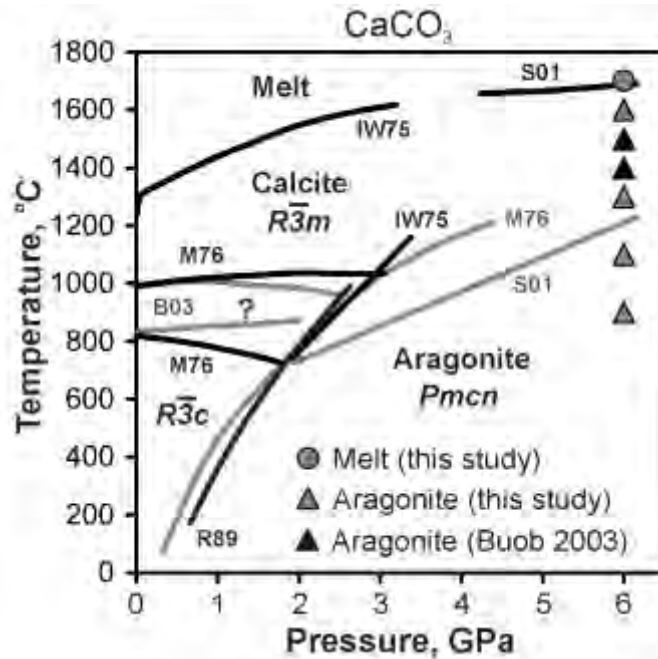
Fig. 6. Phase relations in CaCO₃. IW75 - (Irving and Wyllie 1973); M76 - (Mirwald 1976); R89 - (Redfern et al. 1989); S01 - (Suito et al. 2001); B03 - (Bagdassarov and Slutskii 2003).
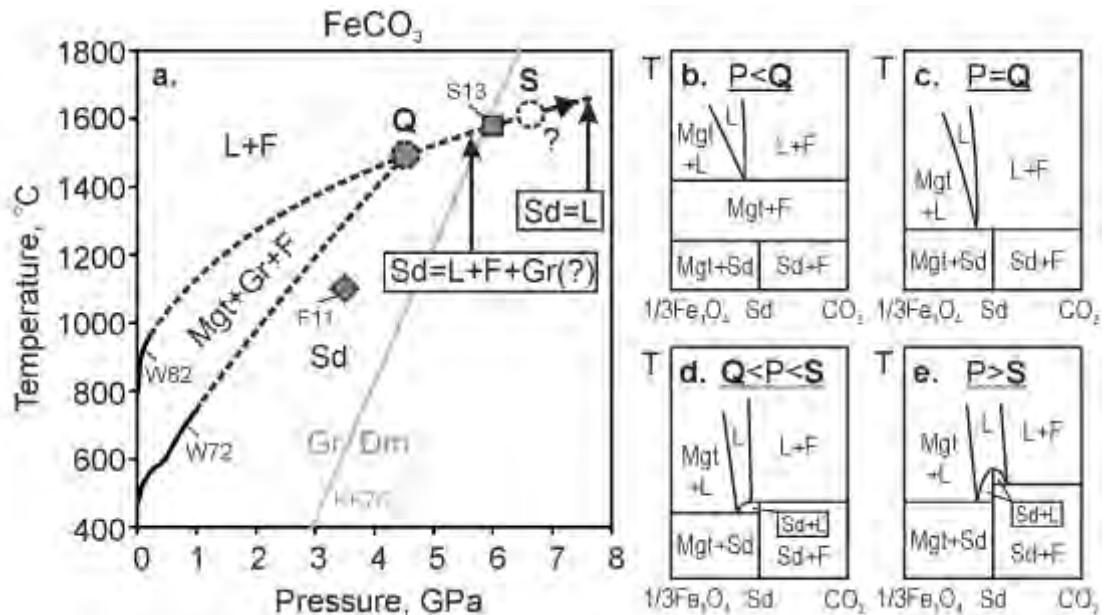
Fig. 7. The sequence of reactions of siderite decomposition reactions, incongruent and congruent melting with increasing pressure based on the experimental data: W72 - (Weidner 1972); W82 - (Weidner 1982); S13 - (Shatskiy et

27

555   al. 2014b). Mgt = magnetite; Gr = graphite; L = liquid; F = CO_2 fluid; Sd = siderite; Q

556   = invariant point, where incongruent melting begins; S = singular point above which

557   congruent melting occurs. Grey rhomb (F11) denotes the reaction $2Fe_{0.75}Ca_{0.25}CO_3$ =

558     $Fe_{0.5}Ca_{0.5}CO_3 + 1/3Fe_3O_4 + 1/6C + 5/6CO_2$ established with temperature increase

559   from 1000 to 1100 ºC at 3.5 GPa in a graphite capsule (Franzolin et al. 2011). Gr/Dm

560   is graphite-to-diamond transition (Kennedy and Kennedy 1976). b-e − Schematic

561   isobaric projections illustrating siderite decomposition and melting expected in the

562   Fe-C-3O system. We assume that graphite is present in excess and skip it on the

563   diagrams.
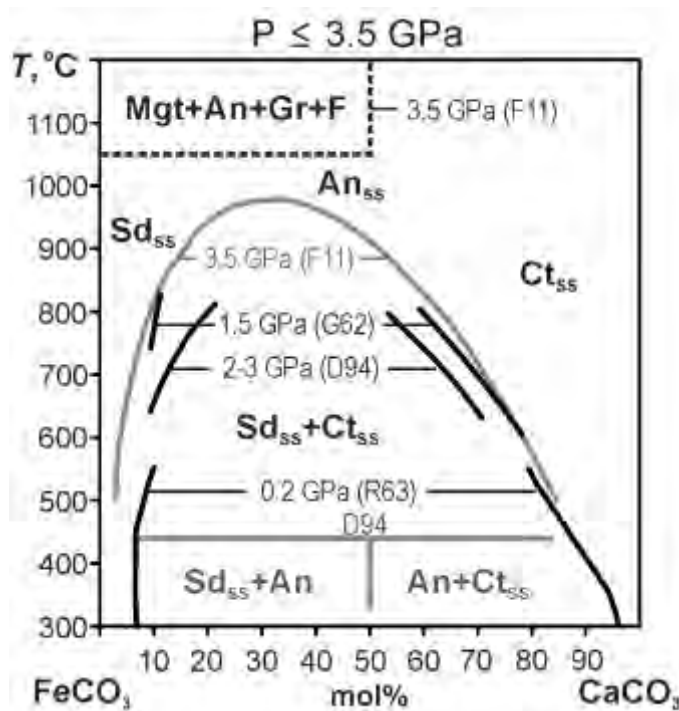
564

565   Fig. 8. Subsolidus phase relations in the pseudobinary system $FeCO_3$-$CaCO_3$ at

566   P ≤ 3.5 GPa: Summary of previous experimental data (black lines) and

567   thermodynamic modeling (grey lines). The numbers in GPa denote the pressure

568   conditions. G62 - (Goldsmith et al. 1962); R63 - (Rosenberg 1963); D94 - (Davidson

569   et al. 1994); F11 - (Franzolin et al. 2011). In their experiments at 3.5 GPa in double

570   Pt-graphite capsules, Franzolin et al. (2011) established complete solid solutions

28

571   between $FeCO_3$ and $CaCO_3$, whereas at 1100 ºC stoichiometric ankerite (An) and

572   magnetite (Mgt) were found at XCa = 25 mol%.
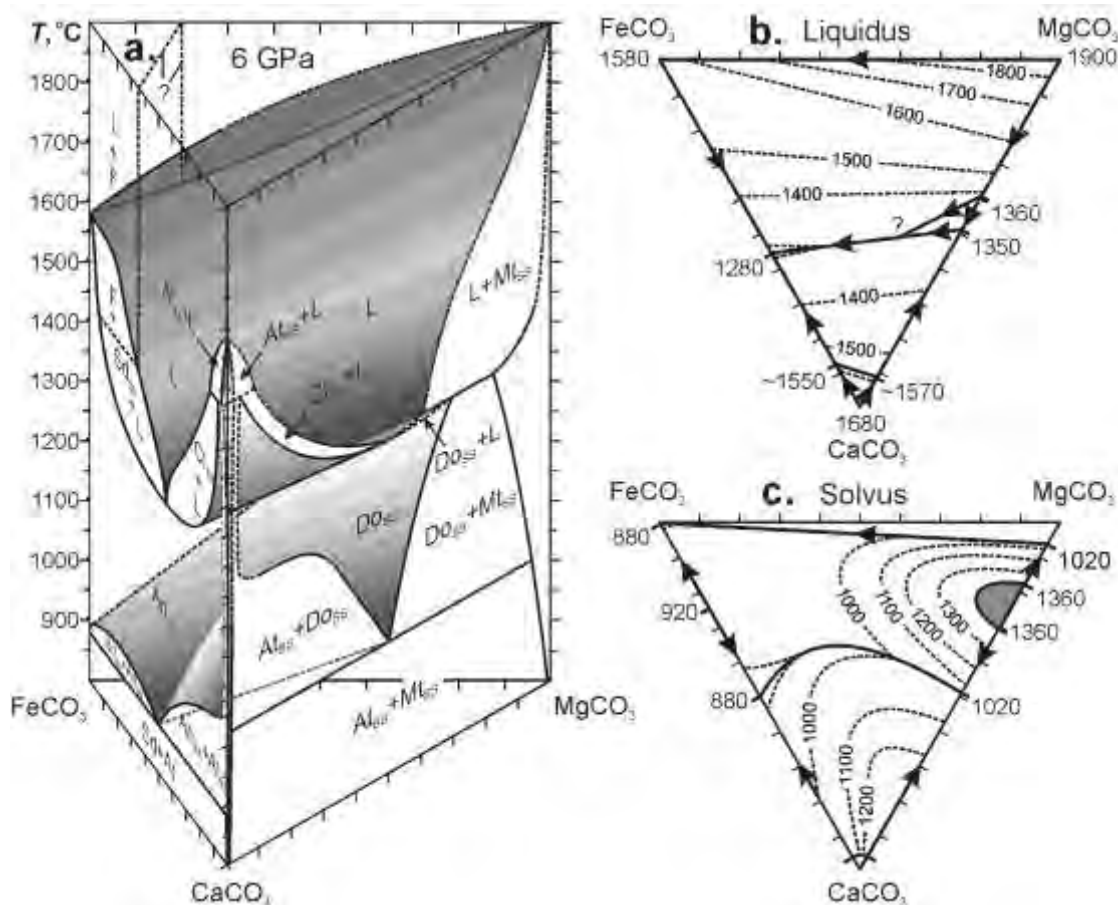
573

574   Fig. 9. Subsolidus and melting phase relations in the pseudo-ternary system

575    $FeCO_3$-$MgCO_3$-$CaCO_3$ at 6 GPa. Sd = siderite; Sd_{SS} = Ca-bearing siderite; An_{SS} =

576   ankerite solid solution; Ct_{SS} = Fe-bearing calcite; At = aragonite; At_{SS} = Fe-bearing

577   aragonite; L = liquid; F = CO_2 fluid. The $CaCO_3$-$MgCO_3$ side is from (Buob 2003).

578   The $FeCO_3$-$MgCO_3$ side is from (Shatskiy et al. 2014b). $MgCO_3$ melting point is from

579   (Katsura and Ito 1990). The numbers on the figures b and c are temperatures in °C.

580

29
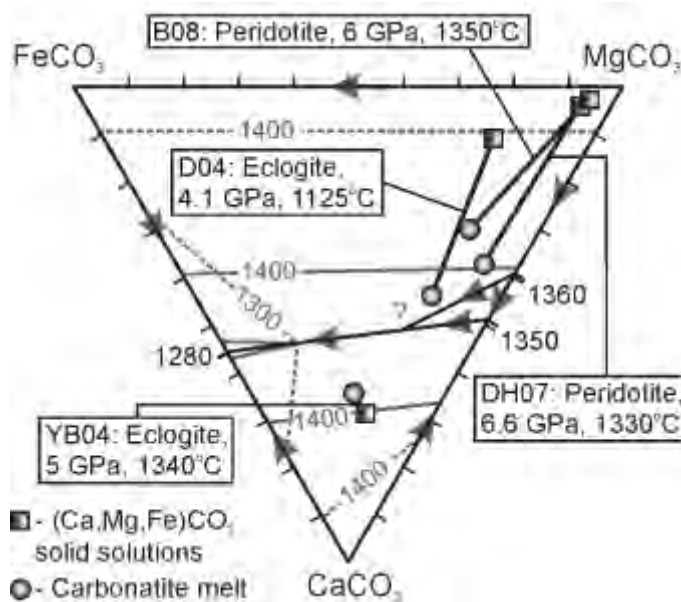
581

582   Fig. 10. Compositions of carbonatite partial melts and coexistent

583   (Ca,Mg,Fe)CO$_3$ solid solutions established in the eclogite-CO$_2$ and peridotite-CO$_2$

584   systems. YB04 = (Yaxley and Brey 2004); D04 = (Dasgupta et al. 2004); B08 = (Brey

585   et al. 2008); DH07 = (Dasgupta and Hirschmann 2007). Grey solid and dottes lines

586   are isoterms on liquidus and solidus surfaces in the CaCO$_3$-MgCO$_3$-FeCO$_3$ system.

587   The numbers denote temperature in °C.

588

30

589   Table. 1. Compositions (mol%) of the run products in the system $(Fe_{0.87}Mn_{0.06}Mg_{0.07})CO_3$-$CaCO_3$ at 6
590   GPa.

#, T, τ		Composition of run products			
XCa	Phases	Ca#	Fe	Mn	Mg
B1032, 900°C, 41 h					
20	An	35.8(2.5)	87.9(6)	5.7(3)	6.4(5)
	Sd	1.6(7)	89.3(1.2)	5.5(7)	5.2(6)
30	An	41.5(6)	88.0(2)	5.6(2)	6.4(2)
	Sd	1.3(2)	89.0(4)	5.1(1.2)	5.9(9)
40	An	42.5(2)	87.8(6)	5.6(4)	6.6(4)
	Sd	2.3(1)	88.1(5)	5.9(5)	6.0(6)
50	An	50.5(7)	88.2(4)	5.6(2)	6.2(3)
60	An	51.5(6)	87.9(5)	5.6(2)	6.5(4)
	At	98.9(2)	100.0	0.0	0.0
70	An	52.1(1)	88.2(4)	5.4(2)	6.4(2)
	At	99.5(2)	100.0(0)	0.0	0.0
80	An	52.3(4)	87.9(1.1)	5.4(0)	6.7(1.1)
	At	99.0(4)	100.0(0)	0.0	0.0
90	An	50.8(8)	88.3(2)	5.2(1)	6.5(3)
	At	100.0(0)	0.0	0.0	0.0
B1033, 1000 °C, 30 h					
10	An	10.3(3)	87.9(3)	5.5(1)	6.6(3)
20	An	20.4(4)	88.0(3)	5.5(3)	6.5(4)
30	An	30.4(5)	87.7(4)	5.7(2)	6.6(4)
40	An	41.3(7)	86.2(1)	5.9(3)	7.9(2)
50	An	51.0(3)	87.8(3)	5.8(1)	6.5(3)
60	An	60.2(7)	86.4(8)	5.4(8)	8.1(3)
70	An	72.0(3)	87.2(6)	5.6(4)	7.2(4)
80	An	78.7(3)	86.1(6)	6.2(5)	7.7(4)
	At	100.0(0)	0.0	0.0	0.0
90	An	78.9(4)	87.1(7)	5.4(7)	7.5(9)
	At	99.5(0)	100.0	0.0	0.0
B1034, 1100 °C, 15 h					
10	An	10.5(2)	87.9(9)	5.5(3)	6.7(6)
20	An	19.8(6)	87.7(2)	5.5(2)	6.8(1)
30	An	30.5(4)	87.8(0)	5.4(1)	6.8(0)
40	An	40.0(2)	87.9(1)	5.4(2)	6.7(3)
50	An	49.6(1)	88.5(2)	5.3(1)	6.2(1)
60	An	59.1(4)	88.4(4)	5.3(4)	6.4(0)
70	An	69.7(2)	88.5(6)	5.5(1)	6.0(8)
80	An	80.5(9)	87.9(6)	5.4(2)	6.7(8)
90	An	90.6(6)	87.0(3)	6.1(3)	6.9(3)
B1551, 1200 °C, 10 h					
0	Sd	0.0	87.1(5)	5.6(2)	7.3(4)
10	An	9.5(3)	87.7(1)	5.5(2)	6.8(2)
20	An	18.7(2)	88.1(2)	5.4(1)	6.5(3)
30	An	29.1(1)	87.8(1)	5.8(2)	6.4(1)
40	An	39.1(3)	88.0(3)	5.5(3)	6.5(2)
50	An	49.7(4)	87.7(3)	5.3(3)	6.9(5)
60	An	60.1(2)	88.3(4)	5.5(3)	6.2(2)
70	An	70.0(5)	87.7(1.1)	5.6(3)	6.7(9)
80	An	80.8(4)	87.2(8)	6.0(2)	6.8(8)
90	An	91.6(2)	87.2(6)	5.8(6)	7.0(6)
B1035, 1300 °C, 2 h					
0	Sd	0.0	87.1(2)	5.7(2)	7.3(1)
10	An	9.7(5)	87.7(3)	5.4(2)	6.9(2)
20	An	21.0(2)	88.0(1)	5.2(1)	6.8(1)
30	An	24.6(2)	87.6(1)	5.4(1)	7.1(0)
	L	48.3	90.2	6.2	3.7
40	An	27.3(3)	87.3(3)	5.6(3)	7.2(5)

31

	L	51.1(4)	91.6(9)	4.6(7)	3.8(3)
50	An	28.9(2)	87.0(6)	5.6(3)	7.3(3)
	L	54.2(2)	91.3(7)	4.6(3)	4.1(4)
60	An	75.2(6)	86.1(6)	6.0(3)	7.9(4)
	L	57.7(1)	90.7(6)	4.7(0)	4.6(5)
70	An	77.5(1)	85.2(1)	6.7(8)	8.1(9)
	L	59.0(6)	90.8(2)	4.4(2)	4.8(1)
80	An	79.7(2)	86.0(6)	6.8(5)	7.2(1)
90	An	91.4(6)	100.0	0.0	0.0

T2075, 1500 °C, 1 h

0	Sd	0.0	87.2(0)	5.8(3)	7.0(3)
10	An	6.4(4)	87.0(4)	5.5(1)	7.5(4)
	L	28.7(3)	91.0(2)	5.5(2)	3.5(0)
20	An	6.7(5)	85.3(1)	5.2(0)	9.4(1)
	L(+F)	29.3(6)	89.3(2)	5.4(2)	5.4(2)
30	An	8.8(2)	84.4(2)	5.2(1)	10.4(3)
	L	31.5(0)	88.6(1)	5.6(5)	5.8(3)
40	L	39.9(1)	88.0(4)	5.6(2)	6.4(0.2)
60	L	60.7(1.5)	88.5(8)	5.2(3)	6.3(5)
90	Ct	94.0(5)	86.9(5)	6.1(5)	7.0(5)
	L	82.0(2)	88.8(1)	4.5(1)	6.7(2)

ES355, 1600 °C, 0.5 h

0	Sid	0.3(2)	86.0(7)	5.7(3)	8.3(8)
	L	0.4(3)	90.3(5)	5.7(3)	4.0(3)
10	An	2.8(1)	84.2(3)	5.1(2)	10.7(4)
	L	20.4(3)	89.0(5)	5.3(4)	5.7(9)
20	An	5.5(1)	84.6(6)	5.3(2)	10.1(6)
	L(+F)	22.1(2)	89.5(4)	5.6(2)	4.9(1)
30	L(+F)	31.4(2)	88.6(3)	5.5(1)	5.9(5)
70	L	66.9(4)	88.3(3)	5.2(2)	6.5(4)
90	At	96.5(2)	100.0(0)	0.0	0.0
	L	89.3(2)	87.0(1.4)	6.3(1.4)	6.7(1.4)
100	At	100.0	0.0	0.0	0.0

ES350, 1620 °C, 4 h

10	An	3.7(2)	86.1(4)	5.4(1)	8.5(5)
	L(+F)	17.9(1)	90.1(5)	6.1(2)	3.8(3)
20	L	21.0	87.2	5.7	7.2
30	L(+F)	30.5(0)	88.6(4)	5.3(1)	6.1(4)
50	L	53.2(8)	87.6(4)	5.9(1)	6.5(5)
60	L	59.6	87.2	5.9	6.9

ES358, 1700 °C, 0.5 h

0	L(+F)	0.1(1)	87.6(0)	5.5(0)	6.9(0)
10	L(+F)	11.3(1)	88.2(1)	5.6(1)	6.2(1)
20	L(+F)	20.2(2)	86.9(2)	5.3(5)	7.8(3)
30	L	29.9(0)	87.9(4)	5.2(0)	7.0(4)
70	L	69.1(2)	87.6(2)	5.3(3)	7.1(5)
80	L	78.7(2)	87.6(1.5)	5.3(4)	7.1(9)
90	L	90.8(1)	86.7(7)	6.3(7)	7.0(6)
100	L	100.0(0)	0.0	0.0	0.0

591 *Notes:* # = run number; τ = run duration; X_{Ca} = CaCO$_3$ content in the system; Ca# = CaCO$_3$ content in
592 run products; Fe = Fe/(Fe+Mn+Mg); Mn = Mn/(Fe+Mn+Mg); Mg = Mg/(Fe+Mn+Mg); Sd = siderite;
593 An = ankerire; At = aragonite; L = liquid. Standard deviations are given in parentheses. Letters in the
594 run number, ES, T and B denote the type of HP apparatus, wedge, DIA and BARS, respectively.
595

32

596

597　Table 2. Main Raman vibrations (cm^{-1}) of Ca-Fe carbonates ($R\bar{3}c$) synthesized in the system
598　$Fe_{0.87}Mn_{0.06}Mg_{0.07}CO_3$-$CaCO_3$ at 6 GPa.

Ca#	T, °C	Main vibrations							
		$2v_2$	v_3	v_1	v_2	v_4	e	L	T
94	1500	1750	1439	1088	no	715	no	283	157
90	1100	1750	1440	1088	875	715	no	284	157
80	1100	1746	1443	1088	873	717	no	284	159
70	1100	1744	1447	1089	874	717	571	285	159
60	1100	1741	1448	1089	873	718	568	284	162
50	1100	1739	1448	1089	872	720	562	283	163
40	1100	1737	1447	1089	871	724	554	280	167
30	1100	1734	1444	1086	867	727	542	279	172
10	1100	1729	1433	1085	867	735	520	282	182
6	1500	1728	1430	1086	866	736	515	285	184
0	1500	1728	1428	1087	868	738	501	286	186
0	1600	1727	1431	1087	868	737	511	288	188

599　*Note*: e - electronic Raman scattering from the Fe^{2+} ion (Rutt and Nicola 1974)

600　Table. 3. Compositions (mol%) of near solidus carbonatite melts and carbonates in eclogite-CO_2 and
601　peridotite-CO_2 systems based on published experimental data.

Lithology	Eclogite									Peridotite					
Phases	Grt+CPx+Co+Ct$_{SS}$+L						Grt+CPx+Mt$_{SS}$+L			Ol+OPc+CPx+Grt+Mt$_{SS}$+L					
Ref.	YB04			H03			D04			B08			DH07		
	5 GPa, 1340°C			6 GPa, 1250°C			4.1 GPa, 1125°C			6 GPa, 1350°C			6.6 GPa, 1330°C		
	SM	Ss	L	SM	L		SM	Ss	L	SM	Ss	L	SM	Ss	L
SiO_2	30.1	0.25	5.16	47.8	0.64		40.2	0.06	5.69	34.3	0.07	15.3	33.5	0.03	6.28
TiO_2	–	–	–	–	–		1.60	0.04	0.18	0.11	0.00	0.38	0.12	0.01	0.26
Al_2O_3	11.7	0.16	1.74	9.28	0.19		6.34	0.04	0.70	1.85	0.00	0.41	1.66	0.01	0.85
Cr_2O_3	–	–	–	–	–		0.04	0.02	0.00	0.13	0.00	0.03	0.07	0.02	0.02
FeO	10.1	6.66	8.46	7.66	5.24		10.6	18.2	12.0	4.93	4.98	10.8	5.72	5.88	6.40
MnO	–	–	–	–	–		0.10	0.01	0.32	0.08	0.18	0.39	0.09	0.11	0.23
MgO	12.4	9.86	9.36	9.54	4.67		19.0	70.7	40.1	49.0	92.3	47.1	49.6	90.0	51.3
CaO	19.4	36.2	32.3	16.2	39.7		13.9	10.7	40.7	3.17	2.38	24.7	3.19	3.88	34.3
Na_2O	0.87	0.22	0.6	2.89	0.06		1.56	0.14	0.29	0.28	0.05	0.73	0.24	0.04	0.35
K_2O	–	–	–	0.01	0.00		0.07	0.09	0.04	0.01	0.00	0.08	0.01	0.01	0.02
CO_2	15.4	–	–	6.20	49.6		6.74	–	–	6.07	–	–	5.80	–	–
H_2O	–	–	–	0.41	–		–	–	–	–	–	–	–	–	–
Ca#	46.3	68.7	64.4	48.6	80.0		31.9	10.8	43.8	5.6	2.4	30.0	5.4	3.9	37.2
Mg#	29.7	18.7	18.7	28.5	9.4		43.7	71.0	43.2	85.8	92.6	57.0	84.8	90.2	55.8
Fe#	24.0	12.6	16.9	22.9	10.6		24.4	18.2	13.0	8.6	5.0	13.0	9.8	5.9	7.0
Ca/Mg	1.56	3.67	3.45	1.70	8.49		0.73	0.15	1.01	0.06	0.03	0.52	0.06	0.04	0.67
Mg/(Mg+Fe)	55.3	59.7	52.5	55.5	47.1		64.1	79.5	76.9	90.9	94.9	81.4	89.7	93.9	88.9

602　*Notes*: SM = starting composition; Ss = (Ca,Mg,Fe)CO_3 solid solutions; Grt = garnet; CPx =
603　clinopyroxen; Co = coesite; Ct$_{SS}$ = calcite solid solutions; L = carbonatite melt; Mt$_{SS}$ = magnesite solid
604　solution; Ol = olivine; OPx = orthopyroxene. YB04 = (Yaxley and Brey 2004). H03 = (Hammouda
605　2003). D04 = (Dasgupta et al. 2004). B08 = (Brey et al. 2008). DH07 = (Dasgupta and Hirschmann
606　2007). Ca# = Ca/(Ca+Mg+Fe); Mg# = Mg/(Ca+Mg+Fe); Fe# = Fe/(Ca+Mg+Fe).
607

608

609　　**References cited**

33

610   Alt, J.C., and Teagle, A.H. (1999) The uptake of carbon duringalteration of ocean
611   crust. Geochimica et Cosmochimica Acta, 63, 1527-1535.
612   Bagdassarov, N., and Slutskii, A. (2003) Phase transformations in calcite from
613   electrical impedance measurements. Phase Transitions, 76, 1015-1028.
614   Boulard, E., Guyot, F., and Fiquet, G. (2012) The influence on Fe content on Raman
615   spectra and unit cell parameters of magnesite–siderite solid solutions. Physics
616   and Chemistry of Minerals, 39, 239-246.
617   Brenker, F.E., Vincze, L., Vekemans, B., Nasdala, L., Stachel, T., Vollmer, C.,
618   Kersten, M., Somogyi, A., Adams, F., Joswig, W., and Harris, J.W. (2005)
619   Detection of a Ca-rich lithology in the Earth's deep (> 300 km) convecting
620   mantle. Earth and Planetary Science Letters, 236, 579-587.
621   Brenker, F.E., Vollmer, C., Vincze, L., Vekemans, B., Szymanski, A., Janssens, K.,
622   Szaloki, I., Nasdala, L., Joswig, W., and Kaminsky, F. (2007) Carbonates from
623   the lower part of transition zone or even the lower mantle. Earth and Planetary
624   Science Letters, 260, 1-9.
625   Brey, G.P., Bulatov, V.K., Girnis, A.V., and Lahaye, Y. (2008) Experimental melting
626   of carbonated peridotite at 6-10 GPa. Journal of Petrology, 49, 797-821.
627   Brey, G.P., Bulatov, V.K., and Girnis, A.V. (2011) Melting of K-rich carbonated
628   peridotite at 6-10 GPa and the stability of K-phases in the upper mantle.
629   Chemical Geology, 281, 333-342.
630   Bulanova, G.P., and Pavlova, L.P. (1987) Magnesite peridotite assemblage in
631   diamond from the Mir pipe. Doklady Akademii Nauk SSSR, 295, 1452-1456.
632   Bulanova, G.P., Walter, M.J., Smith, C.B., Kohn, S.C., Armstrong, L.S., Blundy, J.,
633   and Gobbo, L. (2010) Mineral inclusions in sublithospheric diamonds from
634   Collier 4 kimberlite pipe, Juina, Brazil: subducted protoliths, carbonated melts
635   and primary kimberlite magmatism. Contributions to Mineralogy and
636   Petrology, 160, 489-510.
637   Buob, A. (2003) The system $CaCO_3$-$MgCO_3$: Experiments and thermodinamic solid
638   solutions at high pressure and temperature, Doctor of natural science, p. 109.
639   Swiss Federal Institute of Technology, Zürich.
640   Buob, A., Luth, R.W., Schmidt, M.W., and Ulmer, P. (2006) Experiments on $CaCO_3$-
641        $MgCO_3$ solid solutions at high pressure and temperature. American
642   Mineralogist, 91, 435-440.
643   Byrnes, A.P., and Wyllie, P.J. (1981) Subsolidus and melting relations for the join
644        $CaCO_3$-$MgCO_3$ at 10 kbar. Geochimica Et Cosmochimica Acta, 45, 321-328.
645   Dasgupta, R., Hirschmann, M.M., and Withers, A.C. (2004) Deep global cycling of
646   carbon constrained by the solidus of anhydrous, carbonated eclogite under
647   upper mantle conditions. Earth and Planetary Science Letters, 227, 73-85.
648   Dasgupta, R., and Hirschmann, M.M. (2006) Melting in the Earth's deep upper mantle
649   caused by carbon dioxide. Nature, 440, 659-662.
650   Dasgupta, R., and Hirschmann, M.M. (2007) Effect of variable carbonate
651   concentration on the solidus of mantle peridotite. American Mineralogist, 92,
652   370-379.
653   Dasgupta, R., and Hirschmann, M.M. (2010) The deep carbon cycle and melting in
654   Earth's interior. Earth and Planetary Science Letters, 298, 1-13.
655   Davidson, P.M., Symmes, G.H., Cohen, B.A., Reeder, R.J., and Lindsley, D.H. (1994)
656   Synthesis of the new compound $CaFe(CO_3)_2$ and experimental constraints on
657   the $(Ca,Fe)CO_3$ join. Geochimica Et Cosmochimica Acta, 58, 5105-5109.
658   Dobretsov, N.L., and Shatsky, V.S. (2004) Exhumation of high-pressure rocks of the
659   Kokchetav massif: facts and models. Lithos, 78, 307-318.

34

660   Dobrzhinetskaya, L.F., Eide, E.A., Larsen, R.B., Sturt, B.A., Trønnes, R.G., Smith,
661   D.C., Taylor, W.R., and Posukhova, T.V. (1995) Microdiamond in high-grade
662   metamorphic rocks of the Western Gneiss Region, Norway. Geology, 23, 597-
663   600.
664   Dobrzhinetskaya, L.F., Wirth, R., and Green, H.W. (2006) Nanometric inclusions of
665   carbonates in Kokchetav diamonds from Kazakhstan: A new constraint for the
666   depth of metamorphic diamond crystallization. Earth and Planetary Science
667   Letters, 243, 85-93.
668   Edwards, H.G., Villar, S.E.J., Jehlicka, J., and Munshi, T. (2005) FT–Raman
669   spectroscopic study of calcium-rich and magnesium-rich carbonate minerals.
670   Spectrochimica Acta Part A: Molecular and Biomolecular Spectroscopy, 61,
671   2273-2280.
672   Ford, C.E. (1978) Platinum-iron alloy sample containers for melting experiments on
673   iron-bearing rocks, minerals, and related systems. Mineral Mag, 42, 271-275.
674   Franzolin, E., Schmidt, M.W., and Poli, S. (2011) Ternary Ca–Fe–Mg carbonates:
675   subsolidus phase relations at 3.5 GPa and a thermodynamic solid solution
676   model including order/disorder. Contributions to Mineralogy and Petrology,
677   161, 213-227.
678   Frech, R., Wang, E.C., and Bates, J.B. (1980) The IR and Raman spectra of $CaCO_3$
679   (aragonite). Spectrochimica Acta Part a-Molecular and Biomolecular
680   Spectroscopy, 36, 915-919.
681   Goldsmith, J.R., Graf, D.L., Witters, J., and Northrop, D.A. (1962) Studies in the
682   system $CaCO_3$–$MgCO_3$–$FeCO_3$. 1. Phase relations. 2. A method for major-
683   element spectrochemical analysis. 3. Compositions of some Ferroan dolomites.
684   Journal of Geology, 70, 659-688.
685   Graf, D.L., and Goldsmith, J.R. (1955) Dolomite-magnesian calcite relations at
686   elevated temperatures and CO_2 pressures. Geochimica et Cosmochimica Acta,
687   7, 109-128.
688   Grassi, D., and Schmidt, M.W. (2011) The melting of carbonated pelites from 70 to
689   700 km depth. Journal of Petrology, 52, 765-789.
690   Gudmundsson, G., and Holloway, J.R. (1993) Activity-composition relationships in
691   the system Fe-Pt at 1300 and 1400 ^{o}C and at 1 atm and 20 kbar. American
692   Mineralogist, 78, 178-186.
693   Gunasekaran, S., Anbalagan, G., and Pandi, S. (2006) Raman and infrared spectra of
694   carbonates of calcite structure. Journal of Raman Spectroscopy, 37, 892-899.
695   Hammouda, T. (2003) High-pressure melting of carbonated eclogite and experimental
696   constraints on carbon recycling and storage in the mantle. Earth and Planetary
697   Science Letters, 214, 357-368.
698   Harker, R.I., and Tuttle, O.F. (1955) Studies in the system CaO-MgO-CO_2: Part 2.
699   Limits of solid solution along the binary join, $CaCO_3$-$MgCO_3$. American
700   Journal of Science, 253, 274-282.
701   Harte, B. (2010) Diamond formation in the deep mantle: the record of mineral
702   inclusions and their distribution in relation to mantle dehydration zones.
703   Mineralogical Magazine, 74, 189-215.
704   Hayman, P.C., Kopylova, M.G., and Kaminsky, F.V. (2005) Lower mantle diamonds
705   from Rio Soriso (Juina area, Mato Grosso, Brazil). Contributions to
706   Mineralogy and Petrology, 149, 430-445.
707   Hilton, D.R., Fischer, T.P., and Marty, B. (2002) Noble Gases and Volatile Recycling
708   at Subduction Zones. Reviews in Mineralogy and Geochemistry, 47, 319-370.

35

709   Huang, W.L., and Wyllie, P.J. (1976) Melting relationships in the systems CaO-CO_2
710   and MgO-CO_2 to 33 kilobars. Geochimica Et Cosmochimica Acta, 40, 129-
711   132.
712   Irving, A.J., and Wyllie, P.J. (1973) Melting relationships in CaO-CO_2 and MgO-CO_2
713   to 36 kilobars with comments on CO_2 in the mantle. Earth and Planetary
714   Science Letters, 20, 220-225.
715   Irving, A.J., and Wyllie, P.J. (1975) Subsolidus and melting relationships for calcite,
716   magnesite and the join $CaCO_3$-$MgCO_3$ to 36 kb. Geochimica et Cosmochimica
717   Acta, 39, 35-53.
718   Jarrard, R.D. (2003) Subduction fluxes of water, carbon dioxide, chlorine, and
719   potassium. Geochemistry Geophysics Geosystems, 4, 8905.
720   Johannes, W., and Bode, B. (1978) Loss of iron to the Pt-container in melting
721   experiments with basalts and a method to reduce it. Contributions to
722   Mineralogy and Petrology, 67, 221-225.
723   Joswig, W., Stachel, T., Harris, J.W., Baur, W.H., and Brey, G.P. (1999) New Ca-
724   silicate inclusions in diamonds - tracers from the lower mantle. Earth and
725   Planetary Science Letters, 173, 1-6.
726   Kaminsky, F., Wirth, R., Matsyuk, S., Schreiber, A., and Thomas, R. (2009)
727   Nyerereite and nahcolite inclusions in diamond: evidence for lower-mantle
728   carbonatitic magmas. Mineralogical Magazine, 73, 797-816.
729   Kaminsky, F.V., Zakharchenko, O.D., Davies, R., Griffin, W.L., Khachatryan-
730   Blinova, G.K., and Shiryaev, A.A. (2001) Superdeep diamonds from the Juina
731   area, Mato Grosso State, Brazil. Contributions to Mineralogy and Petrology,
732   140, 734-753.
733   Katsura, T., and Ito, E. (1990) Melting and subsolidus relations in the $MgSiO_3$–
734          $MgCO_3$ system at high pressures: implications to evolution of the Earth's
735   atmosphere. Earth and Planetary Science Letters, 99, 110–117.
736   Kennedy, C.S., and Kennedy, G.C. (1976) The equilibrium boundary between
737   graphite and diamond. Journal of Geophysical Research, 81, 2467-2470.
738   Khokhryakov, A.F., and Pal'yanov, Y.N. (2000) The dissolution forms of diamond
739   crystals in $CaCO_3$ melt at 7 GPa. Geologiya I Geofizika, 41, 705-711.
740   Kiseeva, E.S., Yaxley, G.M., Hermann, J., Litasov, K.D., Rosenthal, A., and
741   Kamenetsky, V.S. (2012) An experimental study of carbonated eclogite at 3.5-
742   5.5 GPa: Implications for silicate and carbonate metasomatism in the cratonic
743   mantle. Journal of Petrology, 53, 727-759.
744   Kiseeva, E.S., Litasov, K.D., Yaxley, G.M., Ohtani, E., and Kamenetsky, V.S. (2013)
745   Melting and phase relations of carbonated eclogite at 9–21 GPa and the
746   petrogenesis of alkali-rich melts in the deep mantle. Journal of Petrology, 54,
747   1555-1583.
748   Klein-BenDavid, O., Logvinova, A.M., Schrauder, M., Spetius, Z.V., Weiss, Y.,
749   Hauri, E.H., Kaminsky, F.V., Sobolev, N.V., and Navon, O. (2009) High-Mg
750   carbonatitic microinclusions in some Yakutian diamonds - a new type of
751   diamond-forming fluid. Lithos, 112, 648-659.
752   Kontoyannis, C.G., and Vagenas, N.V. (2000) Calcium carbonate phase analysis
753   using XRD and FT-Raman spectroscopy. Analyst, 125, 251-255.
754   Korsakov, A.V., and Hermann, J. (2006) Silicate and carbonate melt inclusions
755   associated with diamonds in deeply subducted carbonate rocks. Earth and
756   Planetary Science Letters, 241, 104-118.

36

757   Larsen, R.B., Eide, E.A., and Burke, E.A. (1998) Evolution of metamorphic volatiles
758   during exhumation of microdiamond-bearing granulites in the Western Gneiss
759   Region, Norway. Contributions to Mineralogy and Petrology, 133, 106-121.
760   Laverne, C. (1993) Occurrence of siderite and ankerite in young basalts from the
761   Galapagos spreading center (DSDP Holes 506G and 507B). Chemical
762   Geology, 106, 27-46.
763   Litasov, K.D., and Ohtani, E. (2009) Solidus and phase relations of carbonated
764   peridotite in the system CaO-Al$_2$O$_3$-MgO-SiO$_2$-Na$_2$O-CO$_2$ to the lower mantle
765   depths. Physics of the Earth and Planetary Interiors, 177, 46-58.
766   Litasov, K.D., and Ohtani, E. (2010) The solidus of carbonated eclogite in the system
767   CaO-Al$_2$O$_3$-MgO-SiO$_2$-Na$_2$O-CO$_2$ to 32 GPa and carbonatite liquid in the
768   deep mantle. Earth and Planetary Science Letters, 295, 115-126.
769   Litasov, K.D., Shatskiy, A., Ohtani, E., and Yaxley, G.M. (2013) The solidus of
770   alkaline carbonatite in the deep mantle. Geology, 41, 79-82.
771   Logvinova, A.M., Wirth, R., Tomilenko, A.A., Afanas'ev, V.P., and Sobolev, N.V.
772   (2011) The phase composition of crystal-fluid nanoinclusions in alluvial
773   diamonds in the northeastern Siberian Platform. Russian Geology and
774   Geophysics, 52, 1286-1297.
775   Marty, B., and Tolstikhin, I.N. (1998) CO2 fluxes from mid-ocean ridges, arcs and
776   plumes. Chemical Geology, 145, 233-248.
777   Merrill, R.B., and Wyllie, P.J. (1973) Absorption of iron by platinum capsules in high
778   pressure rock melting experiments American Mineralogist, 58, 16-20.
779   Meyer, H.O.A., and McCallum, M.E. (1986) Mineral inclusions in diamonds from the
780   Sloan kimberlites, Colorado. Journal of Geology, 94, 600-612.
781   Mikhno, A.O., and Korsakov, A.V. (2013) K$_2$O prograde zoning pattern in
782   clinopyroxene from the Kokchetav diamond-grade metamorphic rocks:
783   Missing part of metamorphic history and location of second critical end point
784   for calc-silicate system. Gondwana Research, 23, 920-930.
785   Mirwald, P.W. (1976) A differential thermal analysis study of the high-temperature
786   polymorphism of calcite at high pressure. Contributions to Mineralogy and
787   Petrology, 59, 33-40.
788   Morlidge, M., Pawley, A., and Droop, G. (2006) Double carbonate breakdown
789   reactions at high pressures: an experimental study in the system CaO-MgO-
790   FeO-MnO-CO2. Contributions to Mineralogy and Petrology, 152, 365-373.
791   Murakami, T., Wallis, S., Enami, M., and Kagi, H. (2008) Forearc diamond from
792   Japan. Geology, 36, 219-222.
793   Navon, O. (1991) High internal pressure in diamond fluid inclusions determined by
794   infrared absorption. Nature, 353, 746-748.
795   Okay, A.I. (1993) Petrology of a diamond and coesite-bearing metamorphic terrain:
796   Dabie Shan, China. European Journal of Mineralogy, 5, 659-675.
797   Pal'yanov, Y.N., Sokol, A.G., Borzdov, Y.M., Khokhryakov, A.F., and Sobolev, N.V.
798   (1998) Crystallization of diamond in the CaCO$_3$-C, MgCO$_3$-C and
799   CaMg(CO$_3$)$_2$-C systems. Doklady Akademii Nauk, 363, 230-233.
800   Palyanov, Y.N., Borzdov, Y.M., Khokhryakov, A.F., Kupriyanov, I.N., and Sokol,
801   A.G. (2010) Effect of nitrogen impurity on diamond crystal growth processes.
802   Crystal Growth & Design, 10, 3169-3175.
803   Perraki, M., Proyer, A., Mposkos, E., Kaindi, R., and Hoinkes, G. (2006) Raman
804   micro-spectroscopy on diamond, graphite and other carbon polymorphs from
805   the ultrahigh-pressure metamorphic Kimi Complex of the Rhodope

37

806   Metamorphic Province, NE Greece. Earth and Planetary Science Letters, 31,
807   672-685.
808 Phillips, D., and Harris, J.W. (1995) Geothermobarometry of diamond inclusions
809   from the De Beers pool mines, Kimberley, South Africa. VI Int. Kimberlite
810   Conf.: Extended Abstr., p. 441-442, Novosibirsk, Russia.
811 Redfern, S., Salje, E., and Navrotsky, A. (1989) High-temperature enthalpy at the
812   orientational order-disorder transition in calcite: implications for the
813   calcite/aragonite phase equilibrium. Contributions to Mineralogy and
814   Petrology, 101, 479-484.
815 Rosenberg, P.E. (1963) Subsolidus relations in the system $CaCO_3$-$FeCO_3$. American
816   Journal of Science, 261, 683-689.
817 Rosenberg, P.E. (1967) Subsolidus relations in the system $CaCO_3$-$MgCO_3$-$FeCO_3$
818   between 350° and 550^oC. The American Mineralogist, 52, 787-796.
819 Rutt, H., and Nicola, J. (1974) Raman spectra of carbonates of calcite structure.
820   Journal of Physics C: Solid State Physics, 7, 4522.
821 Sano, Y., and Williams, S.N. (1996) Fluxes of mantle and subducted carbon along
822   convergent plate boundaries. Geophysical Research Letters, 23, 2749-2752.
823 Scheetz, B.E., and White, W.B. (1977) Vibrational spectra of the alkaline earth double
824   carbonates. American Mineralogist, 62, 36-50.
825 Schrauder, M., and Navon, O. (1994) Hydrous and carbonatitic mantle fluids in
826   fibrous diamonds from Jwaneng, Botswana. Geochimica Et Cosmochimica
827   Acta, 58, 761-771.
828 Searle, M., Hacker, B.R., and Bilham, R. (2001) The Hindu Kush Seismic Zone as a
829   Paradigm for the Creation of Ultrahigh‐Pressure Diamond‐and Coesite‐
830   Bearing Continental Rocks. The Journal of Geology, 109, 143-153.
831 Shatskiy, A., Katsura, T., Litasov, K.D., Shcherbakova, A.V., Borzdov, Y.M.,
832   Yamazaki, D., Yoneda, A., Ohtani, E., and Ito, E. (2011) High pressure
833   generation using scaled-up Kawai-cell. Physics of the Earth and Planetary
834   Interiors, 189, 92-108.
835 Shatskiy, A., Gavryushkin, P.N., Sharygin, I.S., Litasov, K.D., Kupriyanov, I.N.,
836   Higo, Y., Borzdov, Y.M., Funakoshi, K., Palyanov, Y.N., and Ohtani, E.
837   (2013a) Melting and subsolidus phase relations in the system Na_2CO_3-
838      $MgCO_3$+-H_2O at 6 GPa and the stability of $Na_2Mg(CO_3)_2$ in the upper mantle.
839   American Mineralogist, 98, 2172-2182.
840 Shatskiy, A., Sharygin, I.S., Gavryushkin, P.N., Litasov, K.D., Borzdov, Y.M.,
841   Shcherbakova, A.V., Higo, Y., Funakoshi, K., Palyanov, Y.N., and Ohtani, E.
842   (2013b) The system K_2CO_3-$MgCO_3$ at 6 GPa and 900-1450 ºC. American
843   Mineralogist, 98, 1593-1603.
844 Shatskiy, A., Sharygin, I.S., Litasov, K.D., Borzdov, Y.M., Palyanov, Y.N., and
845   Ohtani, E. (2013c) New experimental data on phase relations for the system
846   Na_2CO_3-$CaCO_3$ at 6 GPa and 900-1400 ºC. American Mineralogist, 98, 2164-
847   2171.
848 Shatskiy, A., Borzdov, Y.M., Litasov, K.D., Sharygin, I.S., Palyanov, Y.N., and
849   Ohtani, E. (2014a) Phase relationships in the system K_2CO_3-$CaCO_3$ at 6 GPa
850   and 900-1450ºC: implications for the stability of $K_6Ca_2(CO_3)_5$ and
851      $K_2Ca_3(CO_3)_4$ in the upper mantle. American MineralogistUnder review.
852 Shatskiy, A., Litasov, K.D., Ohtani, E., Borzdov, Y.M., and Palyanov, Y.N. (2014b)
853   The systems K_2CO_3-siderite and magnesite-siderite at 6 GPa and their relation
854   to the ternary system K_2CO_3-$FeCO_3$-$MgCO_3$. Contributions to Mineralogy and
855   PetrologyUnder review.

38

856 Shatskiy, A., Ohtani, E., Litasov, K.D., Borzdov, Y.M., and Palyanov, Y.N. (2014c)
857   The system Na_2CO_3-siderite at 6 GPa and its relation to the system Na_2CO_3-
858     $FeCO_3$-$MgCO_3$. American MineralogistUnder review.

859 Shatsky, V.S., Sobolev, N.V., and Vavilov, M.A. (1995) Diamond-bearing
860   metamorphic rocks from the Kokchetav massif (Northern Kazakhstan). In R.G.
861   Coleman, and X. Wang, Eds. Ultrahigh Pressure Metamorphism, p. 427-455.
862   Cambridge University Press.

863 Shatsky, V.S., Ragozin, A.L., and Sobolev, N.V. (2006) Some aspects of
864   metamorphic evolution of ultrahigh-pressure calc-silicate rocks of the
865   Kokchetav Massif. Russian Geology and Geophysics, 47, 105-119.

866 Sobolev, N.V., and Shatsky, V.S. (1990) Diamond inclusions in garnets from
867   metamorphic rocks: a new environment for diamond formation. Nature, 343,
868   742-746.

869 Sobolev, N.V., Kaminsky, F.V., Griffin, W.L., Yefimova, E.S., Win, T.T., Ryan, C.G.,
870   and Botkunov, A.I. (1997) Mineral inclusions in diamonds from the Sputnik
871   kimberlite pipe, Yakutia. Lithos, 39, 135-157.

872 Sokol, A.G., Palyanov, Y.N., Kupriyanov, I.N., Litasov, K.D., and Polovinka, M.P.
873   (2010) Effect of oxygen fugacity on the H_2O storage capacity of forsterite in
874   the carbon-saturated systems. Geochimica et Cosmochimica Acta, 74, 4793–
875   4806.

876 Stachel, T., Harris, J.W., Brey, G.P., and Joswig, W. (2000) Kankan diamonds
877   (Guinea) II: lower mantle inclusion parageneses. Contributions to Mineralogy
878   and Petrology, 140, 16-27.

879 Suito, K., Namba, J., Horikawa, T., Taniguchi, Y., Sakurai, N., Kobayashi, M.,
880   Onodera, A., Shimomura, O., and Kikegawa, T. (2001) Phase relations of
881     $CaCO_3$ at high pressure and high temperature. American Mineralogist, 86,
882   997-1002.

883 Sweeney, R.J. (1994) Carbonatite melt compositions in the Earth's mantle. Earth and
884   Planetary Science Letters, 128, 259-270.

885 Tao, R., Fei, Y., and Zhang, L. (2013) Experimental determination of siderite stability
886   at high pressure. American Mineralogist, 98, 1565-1572.

887 Walter, M.J., Bulanova, G.P., Armstrong, L.S., Keshav, S., Blundy, J.D., Gudfinnsson,
888   G., Lord, O.T., Lennie, A.R., Clark, S.M., Smith, C.B., and Gobbo, L. (2008)
889   Primary carbonatite melt from deeply subducted oceanic crust. Nature, 454,
890   622-630.

891 Walter, M.J., Kohn, S.C., Araujo, D., Bulanova, G.P., Smith, C.B., Gaillou, E., Wang,
892   J., Steele, A., and Shirey, S.B. (2011) Deep Mantle Cycling of Oceanic Crust:
893   Evidence from Diamonds and Their Mineral Inclusions. Sciencexpress.

894 Wang, A., Pasteris, J.D., Meyer, H.O.A., and DeleDuboi, M.L. (1996) Magnesite-
895   bearing inclusion assemblage in natural diamond. Earth and Planetary Science
896   Letters, 141, 293-306.

897 Weidner, J.R. (1972) Equilibria in the system Fe-C-O; Part I, Siderite-magnetite-
898   carbon-vapor equilibrium from 500 to 10,000 bars American Journal of
899   Science, 272, 735-751.

900 Weidner, J.R. (1982) Iron-oxide magmas in the system Fe-C-O. The Canadian
901   Mineralogist, 20, 555-566.

902 Weiss, Y., Kessel, R., Griffin, W.L., Kiflawi, I., Klein-BenDavid, O., Bell, D.R.,
903   Harris, J.W., and Navon, O. (2009) A new model for the evolution of
904   diamond-forming fluids: Evidence from microinclusion-bearing diamonds
905   from Kankan, Guinea. Lithos, 112, 660-674.

39

906   White, W.B. (1974) The carbonate minerals. In V.C. Farmer, Ed. The Infrared Spectra
907   of the Minerals, Mineralogical Society Monograph, p. 227-284. Mineralogical
908   Society, London.
909   Wyllie, P.J., and Tuttle, O.F. (1960) The system $CaO–CO_2–H_2O$ and the origin of
910   carbonatites. Journal of Petrology, 1, 1-46.
911   Wyllie, P.J., and Boettcher, A.l. (1969) Liquidus phase relationships in the system
912          $CaO-CO_2-H_2O$ to 40 kilobars pressure with petrological applications.
913   American Journal of Science, 267, 489-508.
914   Xu, S., Okay, A.I., Shouyuan, J., Sengor, A.M.C., Wen, S., Yican, L., and Laili, J.
915   (1992) Diamond from the Dabie Shan metamorphic rocks and its implication
916   for tectonic setting. Science, New Series, 256, 80-82.
917   Yaxley, G.M., and Green, D.H. (1994) Experimental demonstration of refractory
918   carbonate-bearing eclogite and siliceous melt in the subduction regime. Earth
919   and Planetary Science Letters, 128, 313-325.
920   Yaxley, G.M., and Brey, G.P. (2004) Phase relations of carbonate-bearing eclogite
921   assemblages from 2.5 to 5.5 GPa: implications for petrogenesis of carbonatites.
922   Contributions to Mineralogy and Petrology, 146, 606-619.
923   Zedgenizov, D.A., Ragozin, A.L., Shatsky, V.S., Araujo, D., Griffin, W.L., and Kagi,
924   H. (2009) Mg and Fe-rich carbonate-silicate high-density fluids in cuboid
925   diamonds from the Internationalnaya kimberlite pipe (Yakutia). Lithos, 112,
926   638-647.
927   Zedgenizov, D.A., Ragozin, A.L., Shatsky, V.S., Araujo, D., and Griffin, W.L. (2011)
928   Fibrous diamonds from the placers of the northeastern Siberian Platform:
929   carbonate and silicate crystallization media. Russian Geology and Geophysics,
930   52, 1298-1309.
931   Zedgenizov, D.A., Kagi, H., Shatsky, V.S., and Ragozin, A.L. (2013) Local variations
932   of carbon isotope composition in diamonds from Sao-Luis (Brazil): evidence
933   for heterogenous carbon reservoir in sublithospheric mantle. Chemical
934   Geology, DOI: 10.1016/j.chemgeo.2013.10.033.
935   Zedgenizov, D.A., Shatskiy, A., Ragozin, A.L., Kagi, H., and Shatsky, V.S. (2014)
936   Merwinite in diamond from São Luis, Brazil: a new mineral of the Ca-rich
937   mantle environment. American Mineralogist, Accepted.
938
939

40